OTKA grant K82066

Novel methods for the improvement of medical diagnostics

Final research report

Introduction

The research project has developed algorithms and methods supporting diagnostic and treatment decisions in the fields of medicine as follows:

- Glycaemic control of intensive-care and diabetic patients;
- Medical image reconstruction (SPECT and PET imaging, organ and tissue identification on the images, partial volume effect correction of the images);
- Medical image processing (dental root canal identification).

In the following sections the main research results are briefly summarized. The most relevant publications related to the specific results are referenced and attached to this report. In addition, an annotated list of selected publications is given to help the identification of the most important publications from the relatively long (more than 120 items) full publication list of the project given in the OTKA project reporting system.

Research results summary by field

Glycaemic control of intensive-care patients

Robust control methods have been developed for intensive-care glycaemic treatment and for diabetic patients [2], [6-10].

The STAR (Stochastic TARgeted) protocol has been adopted for insulin-dosing and feeding protocols in Hungary by collaboration with research partners from New Zealand, as well as the models forming the foundation of the algorithms has been adopted for liver transplanted patients [1], [3-5], [11].

The protocols have been validated by clinical trials; several hospitals use the developed protocols in the every-day treatment in Hungary and New Zealand.

Medical image reconstruction

A novel parallel algorithm of real 3D SPECT image reconstruction has been developed providing better image quality than previous reconstructions without increasing the execution time of imaging, thus enabling the clinical application of the results. Novel algorithms for PET image reconstruction has been developed to improve the PET imaging quality. The SPECT reconstruction algorithms have been included into the official reconstruction library of the Mediso Ltd., now available for their customers. The PET algorithms are embedded into the PET detector simulator of Mediso Ltd. user for designing new gamma cameras. [12-17]

Medical image processing:

Novel algorithms for the automated identification of dental root canals and their medial line from different kinds of CT records that provide significant support in the diagnostic decisions. New algorithms suggested for MR brain image segmentation significantly improving the accuracy of the segmentation and reducing the running time of the image processing. The CT image processing methods are used regularly for research tasks at Semmelweis University. [18-21]

Result facts summary

The research results are published in more than 120 referenced and reviewed international publications. One of the participating researchers earned his PhD degree. Significant portion of the theoretical results has been applied in practice. Using the results of the project new research has been initiated, both in international cooperation and with collaboration with Hungarian institutions:

- EU financed FP7-PEOPLE-2012-IRSES - Marie Curie Action: eTime - Engineering Technology-based Innovation in Medicine (Project reference: 318943);
- Hungarian R&D projects: PETMRI7T – Development of a multimodal PET/MRI imaging device (grant id: 1/2014-VKSZ_14);
- Hungarian basic research project: OTKA K116574: Stochastic models for next generation accurate model-based glycaemic control in intensive care: from all new models and methods to clinical validation.

Selected list of publications by topics
(full publication list of the projekt is given in the OTKA reporting system)

Glycaemic control of intensive-care patients

[1] T Ferenci, B Benyó, L Kovács, L Fisk, G M Shaw, G J Chase: Daily Evolution of Insulin Sensitivity Variability with Respect to Diagnosis in the Critically Ill, PLOS ONE 8: (2) 1-9, 2013

[2] Kovács Levente, Almássy Zsuzsanna, Felszeghy Enikő, Kocsis Győző, Wudi Krisztina, Madarász Eszter, Fövényi József, Körner Anna, Benyó Balázs, Benyó Zoltán, Barkai László: Quasi In-Silico Simulation Results of a Robust Blood glucose control algorithm, DIABETES TECHNOL THE 13: (2) 242, 2011

[3] J Homlok, J G Chase, B Benyo: Variability of Model based Insulin Sensitivity in Liver Transplanted Patients, In: [S n] (szerk.) (szerk.) Preprints of the 19th IFAC World Congress. Cape Town: IFAC, 2014. pp. 11595-11598., 2014

[4] Balázs Benyó, Illyés Attila, Szabó Némedi Noémi, Le Compte Aaron J, Havas Attila, Kovács Levente, Fisk Liam, Shaw Geoffrey M, Chase J Geoffrey: Pilot Study of the SPRINT Glycemic Control Protocol in a Hungarian Medical Intensive Care Unit., JOURNAL OF DIABETES SCIENCE AND TECHNOLOGY 6:(6) pp. 1464-1477. (2012), 2012

[5] Homlok J, Chase JG, Doktor T, Benyo B: Analysis of blood glucose dynamics in liver transplantation: A model-based approach, BIOMED TECH 59: S952-S955, 2014

[6] L. Kovács, Zs. Almássy, E. Felszeghy, Gy. Kocsis, K. Wudi, E. Madarász, J. Fövényi, A. Körner, B. Benyó, Z. Benyó, L. Barkai: Quasi In-Silico Simulation Results of a Robust Blood glucose control algorithm, Diabetes Technology & Therapeutics (Abstracts of 4th International Conference on Advanced Technologies & Treatment for Diabetes, London, UK), vol. 13, no. 2, pp. 242, DOI, 2011

[7] Kovács Levente, Benyó Balázs, Bokor József, Benyó Zoltán: Induced L2-norm Minimization of Glucose-Insulin System for Type I Diabetic Patients, COMPUT METH PROG BIO 102: (2) 105-118, 2011

[8] L. Kovács, Z. Benyó, A. Kovács, B. Benyó: New principles and adequate robust control methods for artificial pancreas, in: Studies in Computational Intelligence, I. Rudas, J. Fodor, J. Kacprzyk, Springer Verlag, DOI: 10.1007/978-3-642-15220-7_7, pp. 75-86, ISBN 978-3-642-15219-1, 2010

[9] L. Kovács, B. Paláncz, E. Borbély, Z. Benyó, B. Benyó: Robust Control Algorithms for Blood-Glucose Control using Mathematica, Acta Electrotechnica et Informatica, vol. 10 (2), pp. 10-15, ISSN 1335-8243, 2010

[10] A. György, P. Szalay, Z. Benyó, B. Benyó, A. Kovács, L. Kovács: ANFIS regulated type 1 diabetic model for different glucose absorption scenarios, INES 2010 – 14th IEEE International Conference on Intelligent Engineering, Gran Canaria, Spain, pp. 327-332, ISBN 978-1-4244-7651-0, 2010

[11] L. Kovács, A. György, P. Szalay, B. Benyó, Z. Benyó, C.E. Hann, J.G. Chase: Investigating the Applicability of LPV Control Theory to ICU Models for Glycaemic Control, CONTROL 2010 – UKACC International Conference on Control 2010, Coventry, UK, pp. 577-582, ISBN 978-184600-0386, 2010

Medical image reconstruction

[12] Szlávecz Ákos, Benyó Balázs: Practical estimation method of the optimal scanning protocol for 180° data acquisition in parallel SPECT imaging, BIOMED SIGNAL PROCES 12: 19-27, 2014

[13] Gábor Hesz, Ákos Szlávecz, Balázs Benyó: Optimization of an iterative SPECT reconstruction algorithm utilizing a partial volume effect correction method, In: A Szakal (szerk.) (szerk.) 2013 IEEE 17th International conference on Intelligent Engineering Systems: INES 2013. Piscataway: IEEE, 2013. pp. 1-5.

[14] Szlávecz Ákos, Hesz Gábor, Bükki Tamás, Kári Béla, Benyó Balázs: GPU-Based Acceleration of the MLEM Algorithm for SPECT Parallel Imaging with Attenuation Correction and Compensation for Detector Response., In: Proceedings of the 18th IFAC World Congress. Milánó, Olaszország, 2011.08.28-2011.09.02. pp. 6195-6200.(ISBN: 978-3-902661-93-7)

[15] Ákos Szlávecz, Gábor Hesz, Tamás Bükki, Béla Kári, Balázs Benyó: Partial volume effect correction methods in single photon emission computed tomography., INTERNATIONAL JOURNAL OF COMPUTER ASSISTED RADIOLOGY AND SURGERY 6:(Suppl 1) pp. S351-S352. (2011), 2011

[16] Szlávecz Á, Bükki T, Steinbach C, Benyó B: A novel model-based PET detector block simulation approach, BIOMED SIGNAL PROCES 6: (1) 27-33, 2011

[17] Steinbach Cecilia, Bükki Tamás, Szlavecz Ákos, Benyó Balázs, Lőrincz Emőke: Validation of Detect2000-Based PetDetSim by Simulated and Measured Light Output of Scintillator Crysta Pins for PET Detectors, IEEE T NUCL SCI 57: 2460, 2010

Medical image processing

[18] Balázs Benyó: Identification of dental root canals and their medial line from micro-CT and cone-beam CT records, BIOMED ENG ONLINE 11: (1) , 2012

[19] Szilágyi L, Szilágyi S M, Benyó B: Efficient inhomogenity compensation using fuzzy c-means clustering models, COMPUT METH PROG BIO 108: (1) 80-89, 2012

[20] Szilágyi László, Szilágyi Sándor M, Benyó Balázs, Benyó Zoltán: Intensity inhomogeneity compensation and segmentation of MR brain images using hybrid c-means clustering models, BIOMED SIGNAL PROCES 6: (1) 3-12, 2011

[21] Szilágyi L, Lefkovits L, Iantovics BL, Iclanzan D, Benyó B: Automatic Brain Tumor Segmentation in Multispectral MRI Volumetric Records, LECT NOTES COMPUT SCI 9492: 174-181, 2015

OPEN ACCESS Freely available online

PLOS ONE

Daily Evolution of Insulin Sensitivity Variability with Respect to Diagnosis in the Critically Ill

Tamás Ferenci[1], Balázs Benyó[1], Levente Kovács[1]*, Liam Fisk[2], Geoffrey M. Shaw[3], J. Geoffrey Chase[2]

1 Department of Control Engineering and Information Technology, Faculty of Electrical Engineering and Informatics, Budapest University of Technology and Economics, Budapest, Hungary, **2** Department of Mechanical Engineering, Centre for Bio-Engineering, University of Canterbury, Christchurch, New Zealand, **3** Department of Intensive Care, Christchurch Hospital, Christchurch School of Medicine, University of Otago, Christchurch, New Zealand

Abstract

Introduction: This study examines the likelihood and evolution of overall and hypoglycemia-inducing variability of insulin sensitivity in ICU patients based on diagnosis and day of stay.

Materials and Methods: An analysis of model-based insulin sensitivity for $n=390$ patients in a medical ICU (Christchurch, New Zealand). Two metrics are defined to measure the variability of a patient's insulin sensitivity relative to predictions of a stochastic model created from the same data for all patients over all days of stay. The first selectively captures large increases related to the risk of hypoglycemia. The second captures overall variability. Distributions of per-patient variability scores were evaluated over different ICU days of stay and for different diagnosis groups based on APACHE III: operative and non-operative cardiac, gastric, all other. Linear and generalized linear mixed effects models assess the statistical significance of differences between groups and over days.

Results: Variability defined by the two metrics was not substantially different. Variability was highest on day 1, and decreased over time ($p<0.0001$) in every diagnosis group. There were significant differences between some diagnosis groups: non-operative gastric patients were the least variable, while cardiac (operative and non-operative) patients exhibited the highest variability.

Conclusions: This study characterizes the variability and evolution of insulin sensitivity in critically ill patients, and may help inform the clinical management of metabolic dysfunction in critical care.

Citation: Ferenci T, Benyó B, Kovács L, Fisk L, Shaw GM, et al. (2013) Daily Evolution of Insulin Sensitivity Variability with Respect to Diagnosis in the Critically Ill. PLoS ONE 8(2): e57119. doi:10.1371/journal.pone.0057119

Editor: Frank Emmert-Streib, Queen's University Belfast, United Kingdom

Received November 15, 2012; **Accepted** January 17, 2013; **Published** February 21, 2013

Funding: This research work was supported by the Hungarian National Scientific Research Foundation (http://www.otka.hu/), Grants No. CK80316 and K82066, and it is connected to the scientific program of the "Development of quality-oriented and harmonized R+D+I strategy and functional model at BME" project, supported by the New Hungary Development Plan (Project ID: TAMOP-4.2.1/B-09/1/KMR-2010-0002). Levente Kovacs is supported by the Janos Bolyai Research Scholarship of the Hungarian Academy of Sciences. The funders had no role in study design, data collection and analysis, decision to publish, or preparation of the manuscript.

Competing Interests: The authors have declared that no competing interests exist.

* E-mail: lkovacs@iit.bme.hu

Introduction

Stress induced hyperglycemia is a significant issue in critical care, affecting up to 30–50% of patients and increasing morbidity and mortality [1,2]. Controlling glycemia has proved difficult due to the associated risk of hypoglycemia when highly dynamic patients are treated with exogenous insulin [3]. Both extremes, as well as glycemic variability, have been independently linked to increased morbidity and mortality [4–6], creating a difficult clinical problem.

More specifically, inter- and intra- patient metabolic variability drive outcome glycemic variability and hypoglycemic risk [7] making good control difficult. In particular, sudden and large rises in insulin sensitivity can result in a hypoglycemic event when exogenous insulin is given over a typical 3–4 hour measurement interval. It is critical to determine the size and likelihood of these intra-patient variations, to enable a more complete understanding of the inherent risks in glycemic control.

Very few studies have examined time-varying evolution of insulin sensitivity and its variability in the critically ill. Langouche et al noted [8] that insulin sensitivity rose between days 1 and 5 over their large cohorts, but provided no daily or diagnostic specific evolution. Lin et al showed [9] that hour to hour changes for a clinically validated model-based insulin sensitivity metric could be quite large as a function of current insulin sensitivity level for a medical Intensive Care Unit (ICU) cohort that covered all diagnostic categories and days of ICU stay. However, no studies to date have explicitly described the evolution of intra-patient insulin sensitivity and its variability on a daily basis, or for different diagnostic categories.

Such information would provide insight into the risk of hypoglycemia by diagnostic category and day of ICU stay. Additionally, insight into the likelihood of glycemic variability resulting from greater or lesser intra-patient variability of insulin sensitivity could be attained. This research presents a first rigorous

Table 1. Demographic data of patients.

Group	Day 1			Day 2		
	n	Age	Sex	*n*	Age	Sex
NOpC	28	59.5 (61.5) ± 16.5 (24)	35.7	18	58.4 (59.5) ± 16.1 (19)	38.9
OpC	35	72.9 (73) ± 7.12 (10.8)	22.9	21	72.9 (73) ± 6.54 (10)	23.8
NOpG	16	64.3 (67) ± 12.8 (15)	25	13	64.4 (71) ± 14.2 (18.5)	23.1
OpG	42	67.9 (72) ± 12.4 (13)	35.7	29	69.9 (72) ± 10.8 (11.3)	27.6
NOpO	119	54.7 (59) ± 18 (27)	46.2	101	54.5 (59) ± 18 (28)	42.6
OpO	21	50.8 (56) ± 19.2 (31)	38.1	16	54.9 (57.5) ± 18.5 (31)	43.8
Group	**Day 3**			**Day 4+**		
	n	Age	Sex	*n*	Age	Sex
NOpC	11	64.2 (63) ± 10.6 (16.3)	18.2	11	64.2 (63) ± 10.6 (16.3)	18.2
OpC	18	73.2 (73.5) ± 6.46 (9)	27.8	18	73.2 (73.5) ± 6.46 (9)	27.8
NOpG	13	64.4 (71) ± 14.2 (18.5)	23.1	13	64.4 (71) ± 14.2 (18.5)	23.1
OpG	23	69.2 (71) ± 9.46 (11.5)	26.1	23	69.2 (71) ± 9.46 (11.5)	26.1
NOpO	88	54.2 (58) ± 17.9 (26.5)	45.5	88	54.2 (58) ± 17.9 (26.5)	45.5
OpO	15	54.7 (57) ± 19.1 (33.5)	40	15	54.7 (57) ± 19.1 (33.5)	40

The distribution (according to length-of-stay and diagnosis group) and the most important demographic indicators of the patients. Data are shown in an *n*, age, percentage of females format, with age statistics arranged in Mean (Median) ± SD (IQR) manner. Columns indicate minimum (and not exact) length-of stay, so the same patient may appear in several cells.

doi:10.1371/journal.pone.0057119.t001

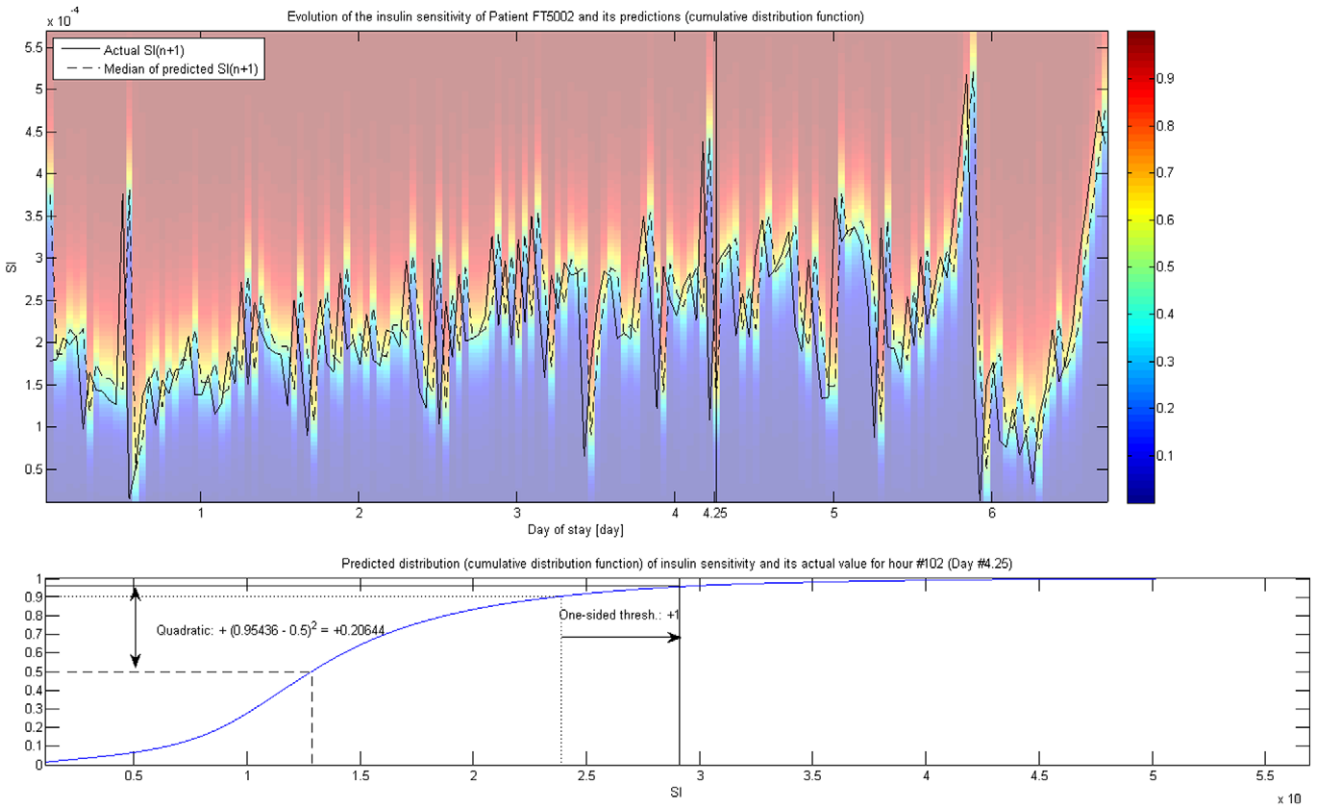

Figure 1. SI **variability and its metrics.** Illustration of the evolution of SI for a given patient (FT5002). Background colors represent the cumulative distribution function of the prediction for $SI(n+1)$ based on $SI(n)$ using the whole cohort; its 25th, 50th (i.e. median) and 75th percentile is explicitly shown. Lower part of the Figure highlights the calculation of the two metrics using Hour #102 (Day #4.25, marked on the upper part) as an example.

doi:10.1371/journal.pone.0057119.g001

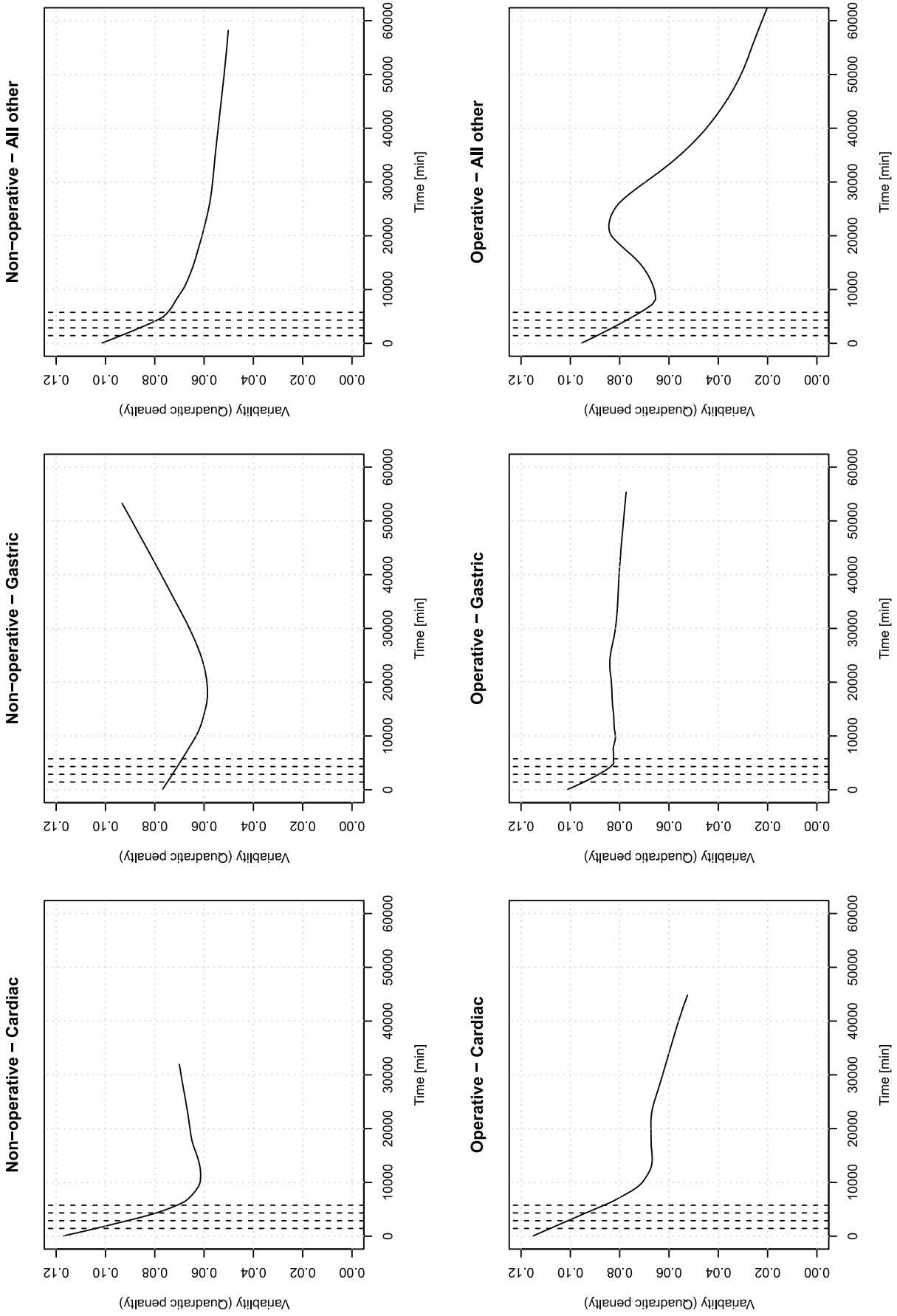
Non−operative − Cardiac
Non−operative − Gastric
Non−operative − All other
Operative − Cardiac
Operative − Gastric
Operative − All other
Variability (Quadratic penalty)
Time [min]
0.00
0.02
0.04
0.06
0.08
0.10
0.12
0
10000
20000
30000
40000
50000
60000

Figure 2. Evolution of quadratic SI variability per diagnosis group. LOWESS estimators for the scatterplot between minute-precision length of stay and quadratic metric of SI variability, segregated according to diagnosis group. Dashed vertical lines indicate the end of the first four days.
doi:10.1371/journal.pone.0057119.g002

statistical analysis of inter- and intra- patient insulin sensitivity variability as a function of diagnostic category and day of stay.

Materials and Methods

Ethics statement

The Upper South Regional Ethics Committee, New Zealand, granted ethics approval for the audit, analysis, and publication of these data. Data collection is described in detail in [10].

Patient data

Clinical data from $n=390$ patients (47,836 hours) in the SPRINT medical ICU cohort [10] are used to identify hourly, model-based insulin sensitivity (SI) values ($SI(n)$). SPRINT is a model-based, clinically validated tight glycemic control (TGC) protocol that provides explicit control for both nutrition intake and insulin input [10].

Hour-to-hour changes are evaluated for the cohort over all days of ICU stay using a stochastic model [9] that provides kernel density estimation-based distributions of $SI(n+1)$ values for each current $SI(n)$ value using all 47,836 data points. Table 1 shows the patient demographic details, including diagnostic categories. These were created based on the APACHE III codes, and consist of operative and non-operative groups for cardiac, gastric and all other patients (with abbreviations OpC, NOpC, OpG, NOpG, OpO and NOpO, respectively). For the daily statistics, only patients who had at least 24 hours of glycemic control and ICU stay were used.

Variability metrics

Actual $SI(n+1)$ values for each day of ICU stay and each diagnostic category (cardiac, gastric, all other, both operative and non-operative in all three types) are compared to the distributions provided by the stochastic model of Lin et al [9] that covers all diagnostic categories and all days of ICU stay. The results thus show the relative and absolute evolution of SI variability ($SI(n)\rightarrow SI(n+1)$) for a given diagnostic category over time, relative to all patients and days of stay, which should highlight times or diagnostic groups with greater or lesser than average risk.

The percentile of the actual $SI(n+1)$ values on their predicted distribution will be illustrated with histograms. If the prediction is perfect (that is, the distribution of actual values is identical to the predicted distribution), every 10% wide interval of the histogram contains 10% of the measurements. This ideal case therefore corresponds to a flat distribution. Kurtic distributions are seen when the actual values were more concentrated at the median than the predicted distribution, suggesting confidence bands could have been tightened. In contrast, U-shaped distributions indicate cases where confidence bands should be widened due to increased variability.

Two metrics are used to assess variability for each patient over a given day, and results are aggregated by diagnostic category. First, a quadratic metric is defined as the average of squared deviations of the percentile of the actual $SI(n+1)$ value on its predicted distribution (from the overall cohort model) from the ideal 50th percentile. This value increases the more variable a given patient. The quadratic metric thus measures overall intra-patient variability.

Second, a one-sided threshold metric counts the number of $SI(n+1)$ values for a given patient that exceed the 90th percentile of $SI(n+1)$ in the whole-cohort model of Lin et al [9]. This metric thus counts the number of large positive changes in $SI(n+1)$ that would induce large drops in glucose level on dosing exogenous insulin based on the $SI(n)$ value. A value greater than 10% for a given patient, day or diagnostic category indicates a greater risk for these changes compared to the overall cohort on all days of ICU stay. This metric thus specifically assesses hypoglycemic risk due to intra-patient variability in insulin sensitivity and its daily evolution.

Hence, these two metrics measure overall variability and hypoglycemic risk from variability. Clinically, the quadratic measure is one of risk to glycemic control performance and outcome arising due to variability in insulin sensitivity, and the one-sided threshold assesses risk to patient safety in glycemic control.

These metrics are illustrated on Figure 1, which shows the evolution of the insulin sensitivity of a 67 years old male patient (FT5002) with septic shock principal diagnosis (all other, non-operative category) through 162 hours. Each patient has such a trajectory. For every hour, the distribution of $SI(n+1)$ was predicted based on $SI(n)$ using the model of Lin et al [9], which is illustrated with the underlying colormap representing the cumulative distribution function of the predicted distribution. 50th percentile (i.e. median) of this predicted distribution of $SI(n+1)$ is explicitly shown. The Figure also illustrates how these metrics are calculated, showing the predicted distribution and the actual SI for a given hour.

Analysis of variability

An overall variability score can be calculated for a given diagnosis group by averaging the overall variability scores for patients belonging to that group. However, if the individual length of stay differs, simple arithmetic averaging would assign unequal weights for each patient's measurements. To avoid the problems associated with unequal weighting due to patient discharge, only series of equal length were averaged. In particular, results and analysis were divided by the first 24 hours ("day 1"), second 24 hours ("day 2"), third 24 hours ("day 3"), and remaining time in ICU ("day 4+"). Thus only complete 24 hour intervals were used (except for day 4+, of course) to avoid bias.

Per-patient average penalty score distributions by diagnosis group each day are shown using violin plots [11]. Violin plots bear similarities to boxplots, but use kernel density estimation to directly convey information on the shape of the distribution for more accurate comparison.

Statistical methods

To have an overall impression on the effect of the time spent in ICU on the SI variability, a LOWESS estimator [12] was plotted for the scatterplot of quadratic metric and time spent (in minutes) per diagnosis group on Figure 2. It is immediately obvious that time has a complex effect on SI variability, which exhibits a biphasic behaviour in most of the cases. This might be worthy of pursuit, despite the fact that the estimation at long length of stays is unreliable due to relatively lower sample size.

However, now we will confine our attention to investigate the early, seemingly mostly linear response of the first few days. (To

NOpC, Day 1 (n=672)
OpC, Day 1 (n=840)
NOpG, Day 1 (n=384)
OpG, Day 1 (n=1008)
NOpO, Day 1 (n=2856)
OpO, Day 1 (n=504)
NOpC, Day 2 (n=432)
OpC, Day 2 (n=504)
NOpG, Day 2 (n=312)
OpG, Day 2 (n=696)
NOpO, Day 2 (n=2424)
OpO, Day 2 (n=384)
NOpC, Day 3 (n=264)
OpC, Day 3 (n=432)
NOpG, Day 3 (n=312)
OpG, Day 3 (n=552)
NOpO, Day 3 (n=2112)
OpO, Day 3 (n=360)
NOpC, Day 4+ (n=677)
OpC, Day 4+ (n=927)
NOpG, Day 4+ (n=1032)
OpG, Day 4+ (n=1066)
NOpO, Day 4+ (n=3386)
OpO, Day 4+ (n=2209)
%
0 5 15
0 20 50 80
Percentile of actual SI(n+1)

Figure 3. Distribution of predictions according to diagnosis and day of stay. Histograms of the percentile of actual $SI(n+1)$ values on their predicted distribution grouped according to day (rows) and diagnosis group (columns). Dashed line indicates the ideal (uniform) case of perfect prediction. The number of hourly measurements which was used to construct the histogram is shown in the title.
doi:10.1371/journal.pone.0057119.g003

illustrate this, the first four day is marked on Figure 2.) We restricted the database to observations having Time $< 8\,000$ minutes (i.e. the first 5.5 days of stay) for the estimation of the forthcoming models, hence limiting it to the "linearity region" of the *SI* variability vs. time function, as evidenced by Figure 2. The linear functional form is also more tractable and easier to estimate.

To account for the grouping of the data, linear mixed-effects modelling was used to find significant differences in *SI* variability metrics between diagnosis groups and/or days [13,14]. The (longitudinal) data were arranged in a two-way classification, with time a within-subject factor and diagnosis group considered a between-subject factor. In our model, the fixed effects were the Time (time spent in ICU in minutes as a continuous variable) and the Diagnosis (as a nominal factor with 6 levels) without intercept ("cell means coding"). Minute-precision length-of-stay (Time) was used for measuring time to make the estimation of the mixed-effects model possible. The random effect was added with per-patient grouping, with both random intercept and random slope permitted with respect to time, both of which was deemed necessary with LR-test ($p<0.001$ for both quadratic and one-sided penalty) [15]. The inclusion of an AR(1) autocorrelation of the within-subject errors was not found to be necessary for the quadratic penalty ($p=0.9961$) [15]. The fixed effects interaction terms between Time and Diagnosis were found to be insignificant ($p=0.8227$ for quadratic penalty, $p=0.2077$ for one-sided penalty) showing that that the slope with respesct to the time spent in ICU does not depend on the diagnosis group, and were thus eliminated. (Effect of Diagnosis was significant ($p<0.0001$ for both penalty), so the intercept does depend on the diagnosis group.) The resulting statistical model for the quadratic penalty of *SI* variability was therefore the following:

$$\begin{aligned} Variability_{i,j} = &\left(\beta_{0,NOpC}\cdot Class_{i,NOpC} + \beta_{0,NOpG}\cdot Class_{i,NOpG} + \dots\right. \\ &\left. + \beta_{0,OpO}\cdot Class_{i,OpO} + b_{0,i}\right) + (\beta_1 + b_{1,i})\cdot Time_{i,j} + \varepsilon_{i,j}, \end{aligned} \quad (1)$$

where i identifies the patient, j identifies the measurement (i.e. $Time_{i,j}$ is the time of the jth measurement on patient i), $Class_{i,C}$ is the indicator variable for Class C (i.e. takes the value of 1 if patient i is in class C, 0 otherwise). For the one-sided threshold penalty – as the response is essentially binary – generalized linear mixed effects (GLME) modeling [16] was used instead of the traditional linear mixed effects (LME) modeling. The link function was chosen to be logistic, and the distribution family was binomial. For the quadratic penalty, LME modeling was used, but the penalty score was (monotonically) logit-transformed beforehand to map the skewed distribution on [0,0.25] to an approximately normal one on the real line [15]. This sacrifies the interpretability of the coefficients for the correct specification of the model, but the former was of little concern for us, as we will not use the numerical values of the coefficients for further analysis. Linearity for the transformed data was still feasible.

The coefficients are denoted with β for the fixed, and with b for the random effects. The fixed effects coefficient of Time characterizes – for the whole population – how variability changes over time, with positive value implying increasing variability, negative implying decreasing variability, and the absolute value showing the size of this effect. The fixed effects coefficients of diagnosis groups show the estimated variability of a patient in the given diagnosis group when admitted to the ICU.

Restricted maximum likelihood (REML) was used for the estimation of LME models and Laplace-approximation for GLME. Residual variance was rather high in both cases, indicating that the models were only able to capture a small part of the variation – but this is to be expected, given that we use no information other than time spent in ICU and diagnosis group.

After performing ANOVA to assess the significance of main effects, post-hoc testing on significant effects was carried out using Tukey's Honestly Significant Differences (HSD) method [17], providing the correction that takes the multiple comparisons situation into account.

Data processing

Data processing was done using Mathworks Matlab (version 2009a). Statistical analysis was performed under the R statistical program package [18], version 2.15.1 with nlme package for LME modeling [19] and lme4 package for GLME modeling [20].

Results

Figure 3 shows the distribution of the percentile of actual $SI(n+1)$ on its predicted distribution for different days and diagnosis groups. Figure 4 shows the violin plot of the distributions of per-patient overall variability metrics in different diagnosis groups, segregated according to ICU day and diagnosis group. Parameters of the fitted GLME model (for one-sided threshold penalty) and LME model (for quadratic penalty) are shown in Table 2.

The distributions in Figure 3 suggest poor coverage of the whole-cohort model on day 1, almost ubiquitously across diagnosis groups. On day 2, every diagnosis group "flattens", except for Operative - Cardiac. On day 3, the predictions are acceptable in every diagnosis group in that the actual distribution of $SI(n+1)$ largely matches the whole cohort-predicted distribution. Finally, on day 4 and onwards the coverage is very over-conservative in the Operative - All other category.

Figure 4 (top row) suggests that one-sided threshold penalties exhibit much larger, typically positively-skewed variations. There is a slight trend in the central tendency, as median variability in this metric appears to decrease as time increases. A trend towards reduced spread in this (one-sided) variability over time is more pronounced, indicating decreasing risk of hypoglycemia over time when all else is equal.

In contrast, quadratic penalties are much more centrally concentrated, and have a smaller coefficient of variation. The continuous lowering of variability over time in every group is also seen, but a reduction in spread is not as pronounced. The two metrics are consistent in assigning "higher" and "lower" variabilities similarly over time and diagnostic group, albeit on different scales.

As can be seen from Table 2, time trend was significant ($p<0.0001$) with a coefficient of -0.1234/day for the one-sided threshold penalty, and -0.1810/day for the (transformed) quadratic penalty, indicating the decreasing variability over time in both cases. These results also imply a decreasing risk of hypoglycemia inducing variability in insulin sensitivity over time, matching trends in Figure 4.

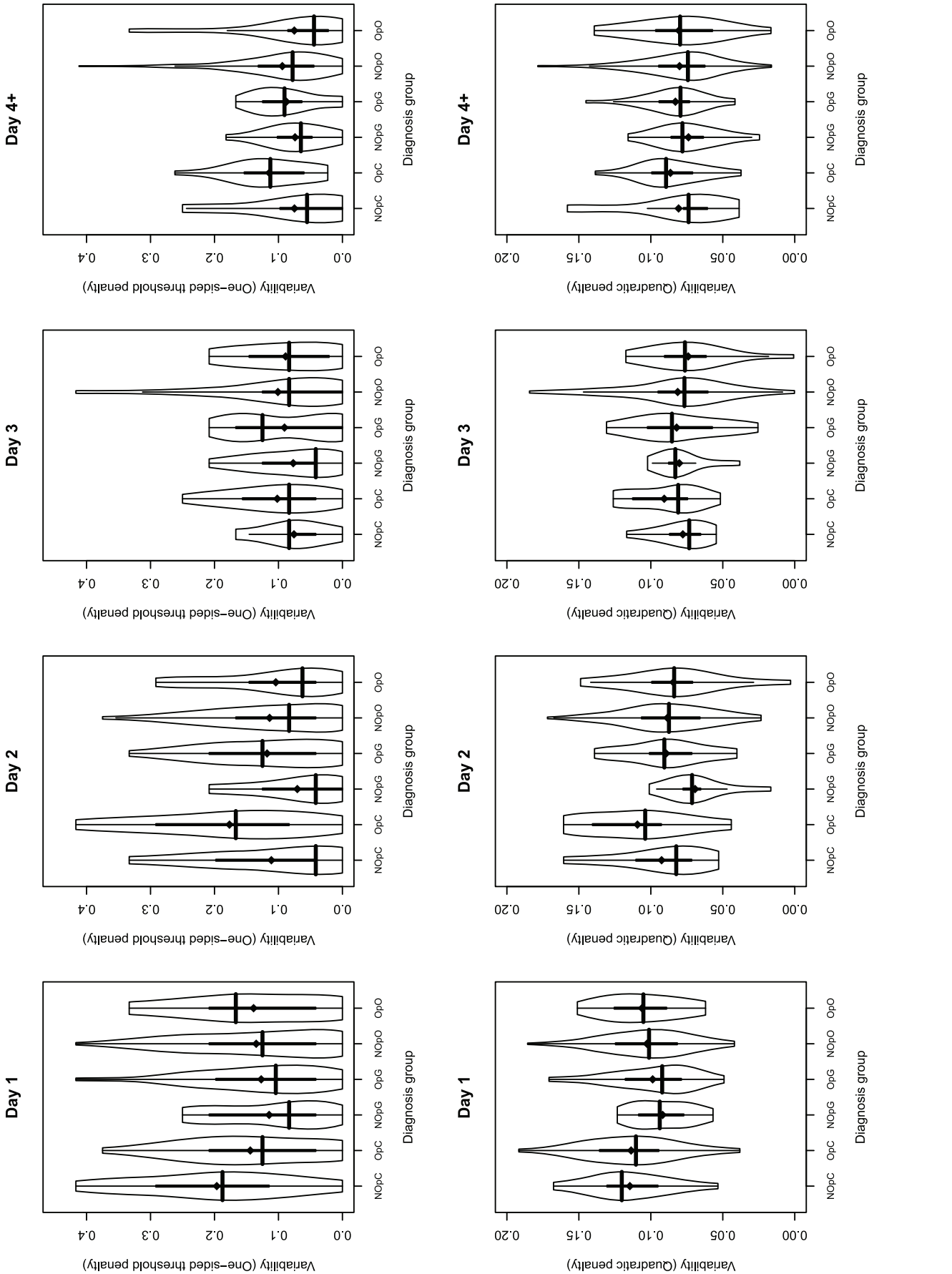
Day 1
Day 2
Day 3
Day 4+
Variability (One−sided threshold penalty)
Variability (Quadratic penalty)
0.0
0.1
0.2
0.3
0.4
0.00
0.05
0.10
0.15
0.20
NOpC
OpC
NOpG
OpG
NOpO
OpO
Diagnosis group

Figure 4. Distribution of per-patient variability scores according to diagnosis and day of stay. Violin plots of per-patient overall variability scores segregated according to day and diagnosis group. Upper row shows one-sided threshold penalty metric, while lower row shows the quadratic penalty metric. Thick vertical lines indicate the interquartile range, the crossing horizontal line is at the median. Dots indicate the mean.
doi:10.1371/journal.pone.0057119.g004

Post-hoc testing for diagnosis groups also revealed significant differences. Using Tukey's HSD method (see Table 3), Non-operative - Cardiac group had significantly ($p = 0.0175$) higher variability than Non-operative - Gastric for the one-sided threshold penalty. Non-operative - All other category also exhibited marginally significantly ($p = 0.0832$) lower SI variability than Non-operative - Cardiac patients. The Operative - Cardiac exhibited significantly ($p = 0.0444$) higher variability than Non-operative Gastric for the (transformed) quadratic penalty. These results suggest that the Non-operative - Gastric group is amongst the least variable groups, while the Cardiac groups exhibit the highest variability irrespective of day. These results are consistent with Figure 4, though it is worth noting that cardiac patients "change place" from day 1 to day 2 irrespective of penalty: Non-operative - Cardiac patients are more variable than Operative - Cardiac group on day 1, but this order is reversed from day 2 onwards.

Discussion

Clinically, those results indicate a decreasing likelihood of hypoglycemia induced by large rises (variations) in insulin sensitivity over short measurement and intervention intervals as days of ICU stay increase based on the one-sided threshold results. The overall risk of increased variability of both forms (one-sided and quadratic metrics) by diagnostic category is highest for Cardiac patient groups.

This latter observation is matching the increased hypoglycemia observed in glycemic control studies in these cohorts (e.g. [21]). The highest variability on day 1 is consistent with the increased hypoglycemia and range observed in the first 24 hours in the study by Bagshaw et al [4], which was associated with increased risk of death. The overall higher variability (quadratic measure) on day 1 in all groups is also reflective of increased hypoglycemia and variability reported in most glycemic control studies irrespective of cohort [3,4].

The major strength of the present study is that it also provides a rigorous statistical framework, which makes the quantification of these effects possible. It is, however, limited in some sense because it is inherently linked to the SPRINT protocol (as it interprets variability as the deviation of the actual SI from its prediction provided by the particular algorithm in that protocol).

The physiological causes of this variability have links to the counter-regulatory and oxidative stress responses, and inflammatory acute immune response typically seen in hyperglycemic critically ill patients. That the variability declines over days 1–4 as the acute phase passes also matches expectations and physiological observations. Drug therapies, such as glucocorticoid or inotrope use [22] among others, may also be implicated as a causative factor. However, the high level of patient-specificity observed within any group makes determining specific causes or magnitude of effect difficult.

For glycemic control, high levels of variability combined with infrequent BG measurement are a major disincentive to higher insulin doses and/or low glycemic targets. The only study to reduce both mortality and hypoglycemia [10] was notable in modulating both insulin and nutrition inputs to achieve good control with lesser insulin and thus reduce hypoglycemic risk. Hence, either higher targets [23] and/or adding nutritional intake into consideration in providing glycemic control [24] must be considered for at least some diagnostic groups (e.g Cardiac patients) and days of ICU stay (day 1) based on these results.

Table 2. Fixed effect coefficients of the fitted models for the one-sided and the quadratic penalty.

Variable	One-sided penalty	(Transformed) Quadratic penalty
Non-operative - Cardiac	−1.5807	−0.5033
Operative - Cardiac	−1.9092	−0.4427
Non-operative - Gastric	−2.3532	−1.048
Operative - Gastric	−1.8791	−0.6922
Non-operative - All other	−1.9903	−0.7350
Operative - All other	−2.0911	−0.8467
Time (per minute)	−0.00008571	−0.0001257
Time (per day)	−0.1234224	−0.1810
	$p < 0.0001$	$p < 0.0001$

Summary of the estimated fixed effect coefficients of the LME model for (logit-transformed) quadratic penalty and the GLME model for the one-sided threshold penalty, and the p-value for the test of significance for Time. The coefficient of Time is given both per minute and per day ($24{\cdot}60 = 1440$ times the former).
doi:10.1371/journal.pone.0057119.t002

Table 3. Significance of the effect of diagnosis group with Tukey-HSD correction for multiple comparisons.

Comparison	One-sided penalty		(Transformed) Quadratic penalty	
	Estimate	p	Estimate	p
OpC - NOpC	−0.3285	0.4188	0.0606	0.9992
NOpG - NOpC	−0.7724	0.0172	−0.5451	0.1505
OpG - NOpC	−0.2984	0.5130	−0.1889	0.8637
NOpO - NOpC	−0.4096	0.0835	−0.2317	0.6190
OpO - NOpC	−0.5104	0.1438	−0.3434	0.5038
NOpG - OpC	−0.4440	0.3607	−0.6057	0.0444
OpG - OpC	0.0300	1.0000	−0.2495	0.4946
NOpO - OpC	−0.0811	0.9890	−0.2923	0.1525
OpO - OpC	−0.1819	0.9335	−0.4040	0.2077
OpG - NOpG	0.4740	0.2765	0.3563	0.5179
NOpO - NOpG	0.3628	0.5024	0.3135	0.5799
OpO - NOpG	0.2621	0.9034	0.2017	0.9539
NOpO - OpG	−0.1112	0.9503	−0.0428	0.9992
OpO - OpG	−0.2120	0.8732	−0.1545	0.9518
OpO - NOpO	−0.1008	0.9919	−0.1117	0.9817

Estimates of differences and the p-values for the test of their significance (using Tukey-HSD post hoc testing for the multiple comparisons situation) for the pairwise comparison of diagnostic categories.
doi:10.1371/journal.pone.0057119.t003

Conclusions

Inter-patient variability in insulin sensitivity peaks on day 1 across diagnostic groups and metrics. Operative - All other patients are more predictable after day 4 than an all patients and days of stay model accounted for, shown by conservative coverage. The distribution of overall intra-patient variability assessed per-patient and the mixed-effects model shows there are distinctive differences between diagnosis groups, irrespective of the time spent in the ICU. In particular, the Non-operative - Gastric group exhibits the smallest variability, while Cardiac groups are amongst the most variable. Clinically, these results show decreasing risk of hypoglycemia as length of stay increases, as well as some reduction in glycemic variability when all else is equal. The overall results can be used to guide the design and implementation of glycemic management specific to diagnosis group and ICU day of stay to improve control and reduce risk.

Author Contributions

Conceived and designed the experiments: TF BB JGC. Analyzed the data: TF LK LF GMS. Wrote the paper: TF LK JGC.

References

1. Krinsley JS (2003) Association between hyperglycemia and increased hospital mortality in a heterogeneous population of critically ill patients. Mayo Clin Proc 78: 1471–1478.
2. McCowen KC, Malhotra A, Bistrian BR (2001) Stress-induced hyperglycemia. Crit Care Clin 17: 107–124.
3. Griesdale DE, de Souza RJ, van Dam RM, Heyland DK, Cook DJ, et al. (2009) Intensive insulin therapy and mortality among critically ill patients: a meta-analysis including nice-sugar study data. CMAJ 180: 821–827.
4. Bagshaw S, Bellomo R, Jacka M, Egi M, Hart G, et al. (2009) The impact of early hypoglycaemia and blood glucose variability on outcome in critical illness. Crit Care 13: R91.
5. Egi M, Bellomo R, Stachowski E, French CJ, Hart G (2006) Variability of blood glucose concentration and short-term mortality in critically ill patients. Anesthesiology 105: 244–252.
6. Krinsley JS (2008) Glycemic variability: a strong independent predictor of mortality in critically ill patients. Crit Care Med 36: 3008–3013.
7. Chase JG, Le Compte AJ, Suhaimi F, Shaw GM, Lynn A, et al. (2008) Implementation and evaluation of the SPRINT protocol for tight glycaemic control in critically ill patients: a clinical practice change. Crit Care 12: R45.
8. Langouche L, Vander Perre S, Wouters PJ, D'Hoore A, Hansen TK, et al. (2007) Effect of intensive insulin therapy on insulin sensitivity in the critically ill. J Clin Endocrinol Metab 92: 3890–3897.
9. Lin J, Lee D, Chase JG, Shaw GM, Le Compte A, et al. (2008) Stochastic modelling of insulin sensitivity and adaptive glycemic control for critical care. Comput Methods Programs Biomed 89: 141–152.
10. Chase JG, Shaw G, Le Compte A, Lonergan T, Willacy M, et al. (2008) Implementation and evaluation of the SPRINT protocol for tight glycaemic control in critically ill patients: a clinical practice change. Crit Care 12: R45.
11. Hintze JL, Nelson RD (1998) Violin plots: A box plot-density trace synergism. Amer Statistician 52: 181–184.
12. Cleveland WS (1979) Robust locally weighted regression and smoothing scatterplots. J Amer Statist Assoc 74: 829–836.
13. Pinheiro JC, Bates DM (2000) Mixed Effects Models in S and S-Plus. New York: Springer.
14. Brown H, Prescott R (2006) Applied Mixed Models in Medicine. New York: Wiley.
15. Fox J, Weisberg S (2011) An R Companion to Applied Regression. Thousand Oaks: Sage.
16. Fritzmaurice GM, Laird NM, Ware JH (2004) Applied Longitudinal Analysis. Hoboken: Wiley-Interscience.
17. Hsu J (1996) Multiple Comparisons: Theory and Methods. Boca Raton: Chapman and Hall/CRC.
18. R Core Team (2012) R: A Language and Environment for Statistical Computing. R Foundation for Statistical Computing, Vienna, Austria. URL http://www.R-project.org/. ISBN 3-900051-07-0.
19. Pinheiro J, Bates D, DebRoy S, Sarkar D, R Core Team (2012) nlme: Linear and Nonlinear Mixed Effects Models. R package version 3.1–104.
20. Bates D, Maechler M, Bolker B (2012) lme4: Linear mixed-effects models using S4 classes. URL http://CRAN.R-project.org/package = lme4. R package version 0.999999-0.
21. Preiser JC, Devos P, Ruiz-Santana S, Mélot C, Annane D, et al. (2009) A prospective randomised multi-centre controlled trial on tight glucose control by intensive insulin therapy in adult intensive care units: the Glucontrol study. Intensive Care Med 35: 1738–1748.
22. Pretty C, Chase JG, Lin J, Shaw GM, Le Compte A, et al. (2011) Impact of glucocorticoids on insulin resistance in the critically ill. Comput Methods Programs Biomed 102: 172–180.
23. Moghissi ES, Korytkowski MT, DiNardo M, Einhorn D, Hellman R, et al. (2009) American as-sociation of clinical endocrinologists and american diabetes association consensus statement on inpatient glycemic control. Diab Care 32: 1119–1131.
24. Suhaimi F, Le Compte A, Preiser JC, Shaw GM, Massion P, et al. (2010) What makes tight glycemic control tight? The impact of variability and nutrition in two clinical studies. J Diabetes Sci Technol 4: 284–298.

Optimization of an iterative SPECT reconstruction algorithm utilizing a partial volume effect correction method

Gábor Hesz
Department of Control Engineering and Information Technology, Budapest University of Technology and Economics, H-1117 Budapest, Magyar tudósok körútja 2., Email:hesz@iit.bme.hu

Ákos Szlávecz
Department of Control Engineering and Information Technology, Budapest University of Technology and Economics, H-1117 Budapest, Magyar tudósok körútja 2., Email:szlavecz@iit.bme.hu

Balázs Benyó
Department of Control Engineering and Information Technology, Budapest University of Technology and Economics, H-1117 Budapest, Magyar tudósok körútja 2., Email:bbenyo@iit.bme.hu

***Abstract*—Single Photon Emission Computed Tomography (SPECT) is a widely used imaging technique in nuclear medicine. In SPECT imaging the Maximum Likelihood Expectation Maximization (MLEM) algorithm is a popular reconstruction technique, although the MLEM based image reconstruction is a time consuming process especially in the case if we use it with attenuation correction and compensation for the distance dependent spatial resolution of the detector. In this research we have developed a new MLEM based iterative SPECT reconstruction algorithm reducing significantly the reconstruction time. The new reconstruction method is divided into two phases. In the phases different spatial resolution of the reconstructed volume is used. In the first phase of the reconstruction we scaled down the original spatial resolution of the detected images in order to decrease the amount of data to process and - simultaneously - decrease the computational complexity of the reconstruction algorithm. In the second phase we increased the spatial resolution of the reconstructed image to the original one. In this phase we applied reverse diffusion based partial volume effect (PVE) correction to partially compensate the negative effects of the low resolution. The method has been tested with mathematical phantoms (with a bullet phantom and with the NCAT phantom) with additional noise. Convergence curves shows that the suggested method is able to reconstruct with similar quality than the high resolution reconstruction while the execution time of the algorithm has been significantly reduced.**

***Index Terms*—SPECT; Iterative reconstruction; MLEM; Partial Volume Effect; PVE correction**

I. Introduction

Single Photon Emission Computed Tomography (SPECT) [1] is a widely used imaging technique in nuclear medicine. During SPECT imaging a radiolabelled substance is injected into the human body. The injected tracer is concentrated in specific parts of the body that are of medical interest for disease detection. A rotating gamma camera is then obtaining 2D views (projection images) of the 3D distribution of the radionuclide at different angular positions (Fig. 1). After data acquisition the 3D distribution of the radioactive substance can be reconstructed using appropriate reconstruction algorithm.

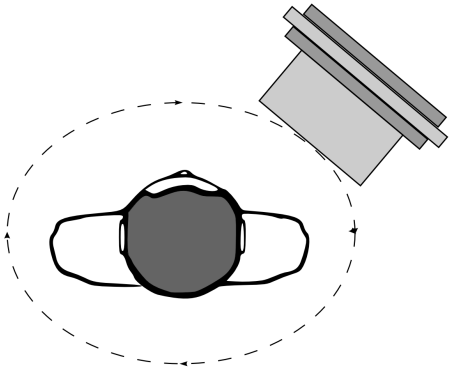

Fig. 1. During SPECT imaging a radionuclide is injected into the body. A gamma camera is rotated around the body and projection images are collected. After data acquisition the 3D distribution of the radioactive substance can be reconstructed using appropriate reconstruction algorithm. [2]

In our recent work, we have developed a fast GPU based iterative SPECT reconstruction algorithm with attenuation correction and compensation for the distance dependent spatial resolution (DDSR) of the detector [2] [3]. The algorithm resulted in an improved spatial resolution and were verified for cardiac perfusion SPECT imaging. A decreased activity around the apical region has been discovered during verification. This apical lesion could be observed systematically on mathematical and physical phantoms as well as on patient studies [3]. This phenomenon is originating from the Partial Volume Effect (PVE).

An evident method to decrease the PVE in SPECT imaging is to reconstruct in higher resolution (i.e. with decreased voxel size). However, using smaller voxels results in a large amount of data to process. Consequently, execution time is significantly increased. Other PVE correction techniques are used pixel based in order to reduce the tissue fraction effect [4] [5] [6].

In this work we developed a reconstruction method that begins with an iterative reconstruction using a given voxel size, then interpolating the volume in a volume with smaller voxel size (high resolution) and at the end iterating in the high resolution volume. With this method result with similar quality has been achieved as processing a reconstruction with a high resolution volume while the execution time is significantly decreased.

II. Methods

A. Maximum Likelihood Expectation Maximization

The Maximum Likelihood Expectation Maximization (MLEM) iterative reconstruction algorithm [7] [8] and its accelerated version using ordered subset [9] is a set of successive forward projections and backprojections where the $(k+1)$ estimation is defined by the following formula:

$$f_j^{k+1} = f_j^k \cdot \frac{1}{\sum_{i=1}^{I} a_{ij}} \cdot \sum_{i=1}^{I} \frac{b_i}{\sum_{n=1}^{J} f_n^k \cdot a_{ni}} \cdot a_{ij} \qquad (1)$$

There are J different image voxels and I detector locations. a_{ij} is the probability that a photon emitted in voxel j is detected in detector location i.

The Poisson probabilistic phenomena of the radioactive decay is taken into account in MLEM. The algorithm calculates the activity distribution which has produced the measured values with the highest likelihood.

The most important distortion effects in SPECT imaging are the gamma photon attenuation in non-homogeneous medium and the distance dependent spatial resolution of the detector (Fig. 2.). In order to achieve a proper reconstruction these effects should be corrected for.

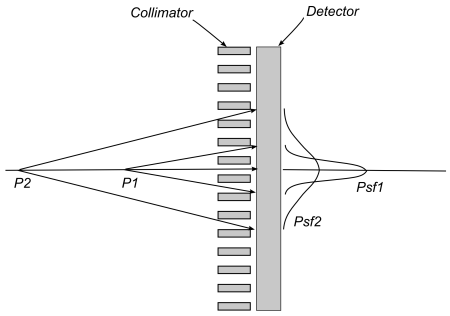

Fig. 2. The gamma camera produce a distance dependent point spread function resulting in a Gaussian blurring. [2]

In the forward projection step we have incorporated the effect of gamma photon attenuation and the distance dependent blurring of the gamma camera [2]. As a consequence of applying these correction in the MLEM, the execution time of the reconstruction algorithm increased extremely. The reconstruction process becomes even more time consuming if high resolution volumes are used.

B. PVE reduction using the reverse diffusion method

The Partial Volume Effect reduction technique by interpolation with revers diffusion is an upscaling method developed originally for Magnetic Resonance Imaging [5].

In this method subvoxels are created and the value of the subvoxels are considered as material that are able to move between subvoxels. The material is allowed to flow towards the highest gradient direction (illustrated in Fig. 3. in 1 dimensional case) resulting in a reverse diffusion process that can be described with a partial differential equation. The reverse diffusion process is highly unstable therefor is controlled by some simple constrained. The method is described in detail in [5].

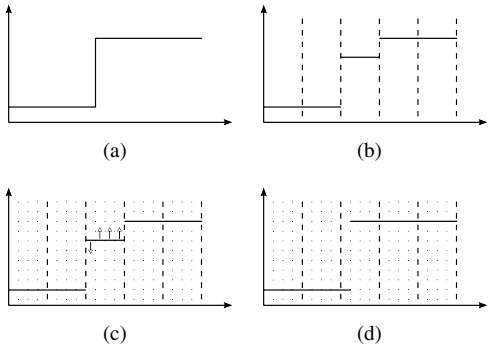

Fig. 3. PVE reduction by interpolation with reverse diffusion is illustrated in 1 dimensional case. (a) is the original signal. (b) is the discretized version of (a) and is suffered from PVE. (c) is the subsampled signal, each value in subvoxels can be increased or decreased. (d) is the result of the reverse diffusion process.

C. Incorporating the PVE reduction technique into MLEM

We have developed a method that utilize the PVE reduction technique while reconstructing the activity distribution in SPECT imaging. The method includes the following steps:

1) doing SPECT data acquisition in high resolution;
2) creating projection images in lower resolution: downscaling the projection images with a factor of 2;
3) reconstructing with 3D MLEM in lower resolution;
4) upscaling the 3D reconstruction volume with a factor of 2 using PVE reduction;
5) continue reconstruction with 3D MLEM in higher spatial resolution (original resolution).

If popular interpolation techniques such as nearest neighbourhood or linear interpolation were used in the method described above the discretization of the lower resolution would remain in the reconstructed image after continuing the reconstruction. Using the PVE correction step in the method similar image quality can achieved while the execution time of the reconstruction process is comparable to the reconstruction with lower resolution.

III. Results and Discussion

The method has been tested with two mathematical phantoms (Fig. 4.). We have created a bullet phantom (Fig. 4

(a)) that has a similar structure like in myocardial perfusion imaging the heart wall. We have used the NCAT phantom [10] that is the exact voxelized model of a human thorax (Fig. 4 (b)).

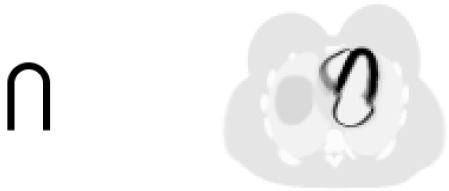

(a) Bullet phantom (b) NCAT phantom

Fig. 4. Mathematical phantoms used in verification. (a): bullet phantom. (b): NCAT phantom.

Projection image series has been generated using the forward projector of our fast GPU based SPECT reconstruction algorithm that involved gamma photon attenuation and DDSR effect. A number of 128 projection images in size of $256x256$ were generated with pixel size of $1mm$. The projection images has been downscaled to $128x128$ size with pixel size of $2mm$.

The projection images in $128x128$ were reconstructed in a 128^3 volume using 40 OSEM iteration, the number of subsets was set to 8. After that the reconstruction volume has been upscaled to $256x256$ size using nearest neighbourhood interpolation, linear interpolation and with PVE reduction technique. Then the reconstruction has been continued in high resolution, 10 has been performed additionally.

In the case of the bullet phantom only the blurring effect of the detector has been simulated while in the case of the NCAT phantom gamma photon attenuation has been also incorporated into the forward projection. The method has been tested in presence of additional Poisson noise.

Convergence curves has been generated while the distance of images in each iteration was calculated according to the following formula:

$$cc = 100 \cdot \left(1 - \left| \frac{C_{1,2}(v_1, v_2)}{\sqrt{C_{1,2}(v_1, v_1) \cdot C_{1,2}(v_2, v_2)}} \right| \right) \quad (2)$$

Where v_1 and v_2 are vectors formed from the two volumes. C is the covariance matrix. The distance calculated this way is invariant to linear scaling.

Reconstructed slices are shown in Fig. 5. It can be seen that the reconstructed slice upscaled with nearest neighbourhood interpolation has lower quality but it is visually not clear whether a linear interpolation or the upscaled with PVE reduction is closer to the 256^3 reconstructed volume. But convergence curves (Fig. 6.) show that using PVE reduction while upscaling the volume result in a "jump" in the convergence curve to the high resolution reconstruction. Using

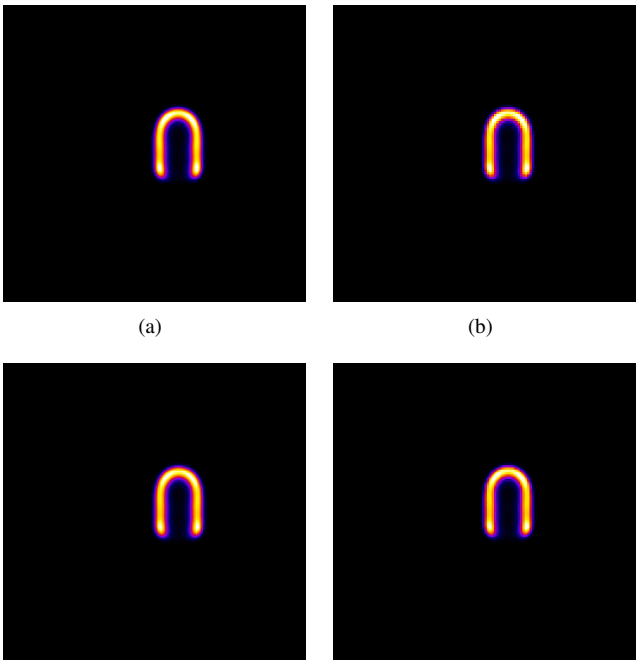

(a) (b) (c) (d)

Fig. 5. Bullet phantom reconstructed slices. (a): 256^3 reconstruction 40 iterations. (b): 128^3 reconstruction, 40 iterations, upscaled with nearest neighbourhood interpolation. (c): 128^3 reconstruction, 40 iterations, upscaled with linear interpolation. (d): 128^3 reconstruction, 40 iterations, upscaled with PVE reduction.

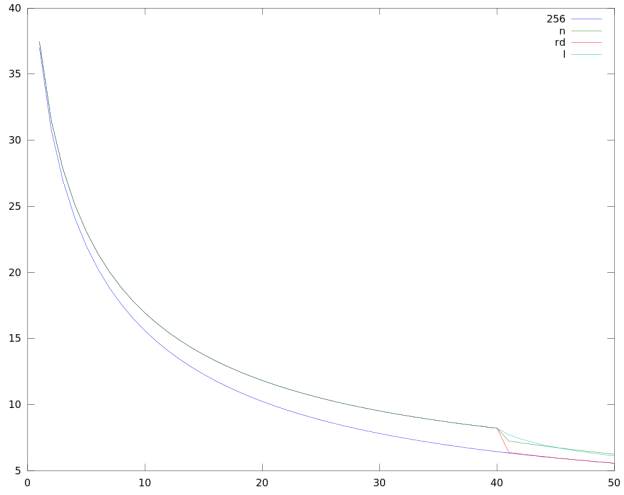

Fig. 6. Bullet phantom convergence curve. Blue: reconstruction in high resolution. Green: reconstructing while upscaling with nearest neighbourhood interpolation. Cyan: reconstructing while upscaling with linear interpolation. Red: reconstructing while upscaling with PVE reduction.

nearest neighbourhood or linear interpolation results in a closer volume but does not reach the high resolution image.

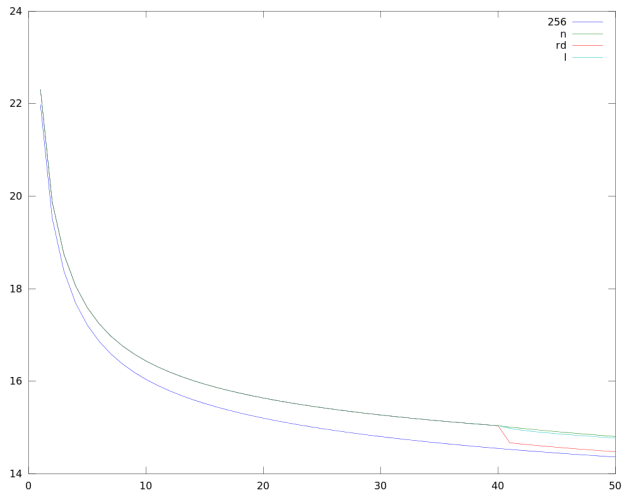

Fig. 7. NCAT phantom convergence curve. Only the detector response has been simulated. Blue: reconstruction in high resolution. Green: reconstructing while upscaling with nearest neighbourhood interpolation. Cyan: reconstructing while upscaling with linear interpolation. Red: reconstructing while upscaling with PVE reduction.

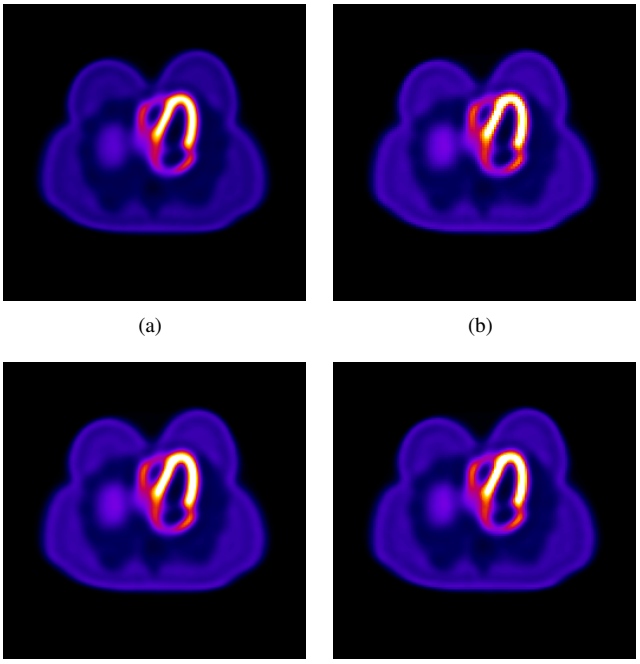

Fig. 8. Bullet phantom reconstructed slices. (a): 256^3 reconstruction 40 iterations. (b): 128^3 reconstruction, 40 iterations, upscaled with nearest neighbourhood interpolation. (c): 128^3 reconstruction, 40 iterations, upscaled with linear interpolation. (d): 128^3 reconstruction, 40 iterations, upscaled with PVE reduction.

The convergence curves of the NCAT phantom simulating only detector blurring is shown in Fig. 7. In this case the convergence curve get closer when PVE reduction is used (but not so much as in case of the bullet phantom) while applying other interpolation techniques does not significantly affect the reconstruction.

The convergence curves of the NCAT phantom simulating detector blurring and gamma photon attenuation as well is shown in Fig. 9. Including the effect of gamma photon attenuation in the simulation does not resulted in a significant difference in the convergence curves. Note that the convergence curves with only detector blurring simulation are running lower. This is because a reconstruction with attenuation correction converges slower. Reconstructed slices show similar result as in the case of the bullet phantom. It can be seen that the reconstructed slice upscaled with nearest neighbourhood interpolation has lower quality but it is visually not clear whether a linear interpolation or the upscaled with PVE reduction is closer to the 256^3 reconstructed volume.

IV. Conclusion

We developed a method that is a combination of the MLEM SPECT reconstruction algorithm and a PVE reduction technique. Applying this method a high resolution reconstruction can be achieved while the execution time is significantly reduced.

The method has been tested with mathematical phantoms while a realistic SPECT system with important distortion effects (gamma photon attenuation and distance dependent

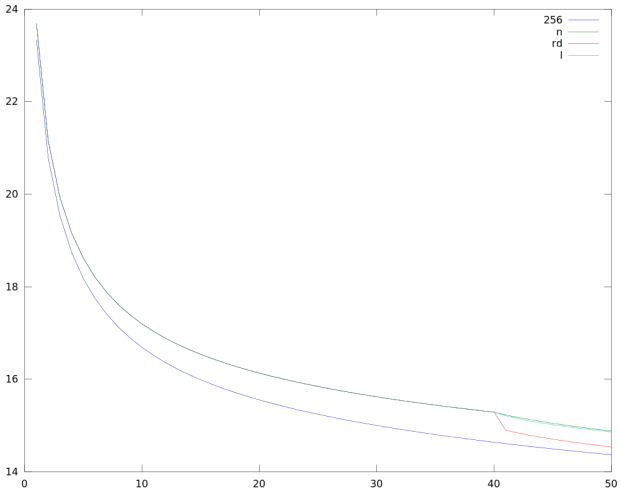

Fig. 9. NCAT phantom convergence curve. Detector response and gamma photon attenuation has been simulated as well. Blue: reconstruction in high resolution. Green: reconstructing while upscaling with nearest neighbourhood interpolation. Cyan: reconstructing while upscaling with linear interpolation. Red: reconstructing while upscaling with PVE reduction.

blurring of the detector) with additional Poisson noise has been simulated. The convergence curves show promising results. In order to prove the applicability of the method further verification with physical phantoms and patient studies should be performed.

Let us note that the suggested method would work with other PVE reduction techniques as well.

ACKNOWLEDGMENT

This work was supported by Mediso Ltd and by the Hungarian National Research Found (OTKA) Grants No. CK80316 and K82066. This work is connected to the scientific program of the "Development of quality-oriented and harmonized R+D+I strategy and functional model at BME" project, supported by the New Hungary Development Plan (Project ID: TÁMOP-4.2.1/B-09/1/KMR-2010-0002). The authors wishes to thank dr. Tamás Bükki for his helpful assistance.

REFERENCES

[1] J. N. A. Miles N. Wernick, *Emission Tomography: The fundamentals of SPECT and PET*. Springer-Verlag London, 2005.

[2] A. Szlávecz, G. Hesz, T. Bükki, B. Kári, and B. Benyó, "GPU-based acceleration of the MLEM algorithm for SPECT parallel imaging with attenuation correction and compensation for detector response," in *Proceedings of the 18th IFAC World Congress. Milan, Italy.*, August 28. - September 2. 2011, pp. 6195–6200.

[3] A. Szlávecz, G. Hesz, Z. Puskás, B. Kári, O. Pártos, T. Györke, T. Bükki, B. Domonkos, and B. Benyó, "A Fast Iterative GPU-based Reconstruction Algorithm for SPECT Imaging Involving Collimator and Attenuation Compensation," *European Journal of Nuclear Medicine and Molecular Imaging*, vol. 37, no. Supplement 2, pp. S284 – S284, October 2010.

[4] N. Boussion, M. Hatt, F. Lamare, Y. Bizais, A. Turzo, C. C.-L. Rest, and D. Visvikis, "A multiresolution image based approach for correction of partial volume effects in emission tomography," *Physics in Medicine and Biology*, vol. 51, no. 7, p. 1857, 2006. [Online]. Available: http://stacks.iop.org/0031-9155/51/i=7/a=016

[5] O. Salvado, C. M. Hillenbrand, and D. L. Wilson, "Partial volume reduction by interpolation with reverse diffusion," *International Journal of Biomedical Imaging*, vol. 2006, pp. 1 – 13, 2006, Article ID 92092.

[6] A. Szlávecz, G. Hesz, T. Bükki, B. Kári, and B. Benyó, "Partial volume effect correction methods in single photon emission computed tomography." vol. 6, no. Supplement 1, 2011, pp. S351 – S352.

[7] K. Lange and R. Carson, "EM reconstruction algorithms for emission and transmission tomography," *Journal of Computer Assisted Tomography*, vol. 8, no. 2, pp. 306–316, April 1984.

[8] L. A. Shepp and Y. Vardi, "Maximum likelihood reconstruction for emission tomography," *Medical Imaging, IEEE Transactions on*, vol. 1, no. 2, pp. 113 –122, oct. 1982.

[9] H. Hudson and R. Larkin, "Accelerated image reconstruction using ordered subsets of projection data," *Medical Imaging, IEEE Trans. on*, vol. 13, no. 4, pp. 601 –609, Dec. 1994.

[10] W. Segars, D. Lalush, and B. Tsui, "A realistic spline-based dynamic heart phantom," *Nuclear Science, IEEE Transactions on*, vol. 46, no. 3, pp. 503 –506, jun. 1999.

BioMedical Engineering OnLine

RESEARCH Open Access

Identification of dental root canals and their medial line from micro-CT and cone-beam CT records

Balázs Benyó

Correspondence:
bbenyo@iit.bme.hu
Budapest University of Technology and Economics, Department of Control Engineering and Information Technology, Magyar tudósok krt. 2, H-1117 Budapest, Hungary

Abstract

Background: Shape of the dental root canal is highly patient specific. Automated identification methods of the medial line of dental root canals and the reproduction of their 3D shape can be beneficial for planning endodontic interventions as severely curved root canals or multi-rooted teeth may pose treatment challenges. Accurate shape information of the root canals may also be used by manufacturers of endodontic instruments in order to make more efficient clinical tools.

Method: Novel image processing procedures dedicated to the automated detection of the medial axis of the root canal from dental micro-CT and cone-beam CT records are developed. For micro-CT, the 3D model of the root canal is built up from several hundred parallel cross sections, using image enhancement, histogram based fuzzy c-means clustering, center point detection in the segmented slice, three dimensional inner surface reconstruction, and potential field driven curve skeleton extraction in three dimensions. Cone-beam CT records are processed with image enhancement filters and fuzzy chain based regional segmentation, followed by the reconstruction of the root canal surface and detecting its skeleton via a mesh contraction algorithm.

Results: The proposed medial line identification and root canal detection algorithms are validated on clinical data sets. 25 micro-CT and 36 cone-beam-CT records are used in the validation procedure. The overall success rate of the automatic dental root canal identification was about 92% in both procedures. The algorithms proved to be accurate enough for endodontic therapy planning.

Conclusions: Accurate medial line identification and shape detection algorithms of dental root canal have been developed. Different procedures are defined for micro-CT and cone-beam CT records. The automated execution of the subsequent processing steps allows easy application of the algorithms in the dental care. The output data of the image processing procedures is suitable for mathematical modeling of the central line. The proposed methods can help automate the preparation and design of several kinds of endodontic interventions.

Background

The shape of the root canal varies from patient to patient, and from tooth to tooth. Severely curved root canals or multi-rooted teeth may pose several challenges in the endodontic treatment. Thus the shape information of root canals can be efficiently used for better intervention planning. Accurate shape information of the root canals may also

be used by manufacturers of endodontic instruments in order to make more efficient clinical tools.

The new 3D imaging technologies like cone-beam computed tomography (CBCT) that are available in more and more dental practices show great promise in this field [1-4] as they make possible the extraction of the dental root canal shape information. However, the development of root canal shape extraction methods raises a set of challenges due to X-ray dose regulations that cause limited image quality [5]. Moreover, in order to design methods to meet the needs of dental practice the image processing methods should be highly automated.

In order to provide an efficient and effective tool that assists endodontic intervention planning, this research focuses on the automatic recognition of the root and root canals and mathematical description of root canal curvatures. The integration of the image processing steps in novel imaging systems may significantly improve endodontic practice in the near future. In addition, the attempt to automatically locate and classify the root canals may result in decreased chair time for both the patient and the practitioner, reducing clinical burden, effort and cost.

Modern medical imaging devices enable recording several cross sections of the teeth, which can be fed to image processing techniques to extract the shape of the root canal. This problem has been solved several different ways, based on recorded data originating from various imaging tools. Analui et al [6] elaborated a geometric approach for modeling and measurement of root canal of human dentition based on stereo digital radiography. Hong et al [7] used 2D radiographic images to build up a 3D tooth model, while Endo et al [8] turned to ultrasonic imaging and implemented a fuzzy logic based root canal detection. Lee et al [9] used micro-CT images and 3D reconstruction software to measure the three-dimensional canal curvature in maxillary first molars via mathematical modeling. Several other 3D dental structure reconstruction systems were elaborated, including Willershausen et al [10] who used X-ray images, and van Soest et al [11], who applied optical coherence tomography records for 3D structure reconstruction. Germans et al [12] presented an imaging system based on virtual reality that can navigate through the reconstructed 3D structure and make measurements concerning the curvature of the root canal.

Recently, further solutions have emerged: Park et al [13] proposed a root canal configuration identification method specialized for the first molar, based on micro-CT records. Neves et al [14] elaborated a quantitative evaluation technique for caries excavation. Evaluation methods for the morphology of the root canal were given by Verma and Love [15], and Yamada et al [16]. The root canal of the incisors were studied by Kaya et al [17], who evaluated the changes in the canal's shape due to aging, and Li et al [18], who investigated the effect of manual instrumentation technique on root canal geometry. Recently elaborated modeling tools suitable for the characterization of root canals were given in [19,20].

For further reading in the topic, the reader is referred to the reviews elaborated by Peters [1], Dong et al [21], and Swain and Xu [2].

Medial lines of tubular structures are often approximated with 3D curve skeletons [22]. Curve skeleton extraction methodology has a strong foundation. Methods based on thinning or boundary propagation iteratively remove so-called simple points (whose presence does not affect the topology), from the surface of the object. This is generally achieved

using a hit-or-miss transform extended to three dimensions [23,24]. Approaches based on distance fields define and compute the minimum distance of each discrete interior point to the surface of the object, an approximate the curve skeleton with the ridges of this distance field [25]. Geometric models generally use a graph-based representation for the approximation of the medial surface or curve of the object [26]. Generalized potential field methods define an internal potential field that differs from the distance field (e.g. electrostatic field generated by placing point charges to all discrete boundary locations [27]), and extract a hierarchical structure composed of critical and saddle points of the field.

3D curve skeletons are composed of loci having at least two closest points on the boundary of the object. This property makes curve skeletons suitable to approximate the center line of the root canal. Curve skeletons preserve the topology of the object, and embody the hierarchy of its components, which is relevant at the detection of bifurcations. In order to suit the needs of dental imaging application, an approach has to be chosen that yields the smoothest curve and shows little sensitivity to slight changes of the object's boundary. For further details on the topic of 3D curve skeletons, the reader is referred to [22], which is an excellent repository of such methods and their properties.

The general shortcoming of all reported methods that they provide solution only for a single - or at most some subsequent - steps of the root canal identification. The integration of the methods into an automated procedure requires significant enhancement of the algorithms.

This paper introduces predominantly automated image processing procedures for the segmentation of teeth and root canals, and identification of the medial line of the root canal, using a fuzzy chain relation and 3D curve skeletons. Two different procedures will be proposed and validated on micro-CT and one for CBCT records, respectively.

Methods

Processing micro-CT records

Dental micro-CT records consist of single channel intensity images, representing high-resolution (1500–3000dpi) scans of parallel cross sections of a certain tooth. A set of images may contain several hundred scanned horizontal planes, which usually are linearly distributed along an axis orthogonal to the scanned planes. The distribution of voxel intensity levels varies from slice to slice, but there are a few rules which most slices obey. In this order, the anatomical structure is reflected by voxel intensities. In normal cases, cross sections contain a light gray spot corresponding to the dentin, usually lighter at its edges (that is because the enamel), possibly surrounding one or more darker regions, which represent the root canal containing soft tissues. The cementum, when visible, is usually somewhat lighter than the dentin. Noise is manifested by granular texture and circular texture visible in the light areas. Figure 1 shows two dental cross sections originating from two different micro-CT records.

The main goal of the proposed image processing procedure is to identify the 3D structure of the root canal built up from the inner darker regions identified from all cross sections. Afterwards, curve that corresponds to the central line is identified and tracked. The detected central line must follow the topology of the root canal, by reflecting its curves and bifurcations.

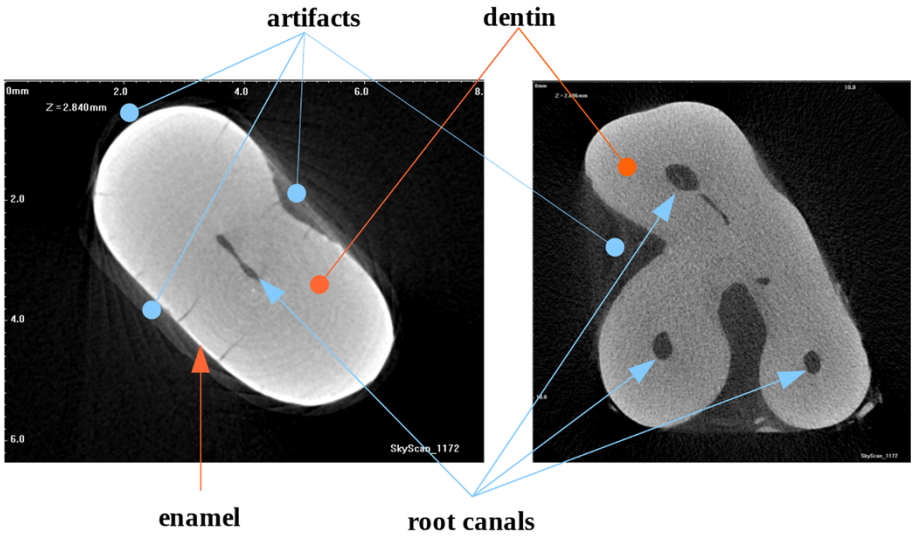

Figure 1 Slices from micro-CT volumes, with typical artifacts.

Figure 2 exhibits the diagram of the image overall processing procedure proposed. The following subsections discuss the functionality of each box of the diagram.

Step MCT1 - Preprocessing

The automatic image segmentation must be preceded by some image enhancement steps. In our application, the following preprocessing steps are employed:

1. A simple median filter, which reduces the high frequency noise that is most visible in the dentin's texture.

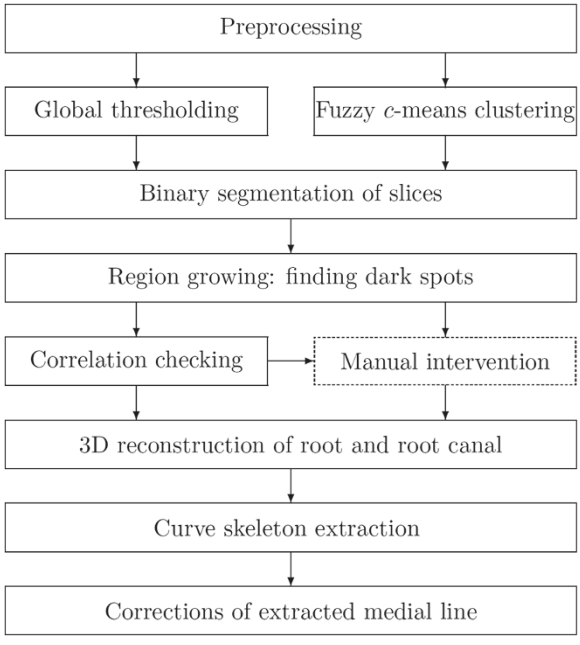

Figure 2 Steps of the proposed algorithm.

2. Establishing the region of interest (ROI) by trimming the image: this way we get rid of the dark areas that represent outer space. It is necessary to store the exact coordinates of the ROI.
3. Some basic morphological operators are used to remove texts from the original image and regularize the boundary of the root canal.

After this preprocessing step, the image is ready for segmentation.

Step MCT2 - Segmentation in 2D

The final result of the planar segmentation should be a binary image. Even if the image enhancement techniques have already suppressed the disturbing textures, high quality segmentation is obtained by applying a double partitioning.

This step produces two different partitions that are both obtained using the histogram based enhanced version (EnFCM) [28] of the fuzzy *c*-means algorithm [29], which partitions the input slice or volume into a predefined number (c) of classes. The first partition is achieved by performing EnFCM on the ROI of the slice, setting the number of clusters to $c = 4$. In the followings, this partition will be referred to as local partition, as it is computed from the local data of the slice. The second partition is produced by a simple thresholding operation, using a previously computed threshold τ_{global} that was obtained by EnFCM from the whole data set, using $c = 2$ clusters. The latter partition is called global partition of the slice, because it uses the global threshold extracted from the data of the whole volume. Theoretically this would involve computing the global histogram. Instead of that, in order to reduce computation time, the global threshold is estimated using only 2% of the slices, which are linearly distributed along the axis.

The global threshold produces a binary image. The local partition contains 4 different colors, corresponding to the prototypes of the 4 clusters, $v_1 \dots v_4$. Let us suppose the intensity values are ordered increasingly, that is, $v_{i+1} > v_i$, $\forall i = 1 \dots c-1$. The 4 clusters are then separated in two classes, using the threshold $\tau_{local} = (v_{i+1} - v_i)/2$, where $i = \arg\max_j \{v_{i+1} - v_i, i = 1 \dots c-1\}$. In most cases, both binary images are good quality partitions, but there are exceptions, when one of these algorithms fails. In these cases the correct partition must be selected.

Step MCT3 - Decision making

To provide an intelligent selection of the correct binary partition, a decision tree has been built based on 250 slices representing above mentioned exceptions. The decision is made in a four dimensional search space, corresponding to parameters: τ_{global}, and $\tau_i = (v_{i+1} - v_i)/2$, where $i = 1 \dots 3$. The output of the tree is the decision whether the local or the global binary partition is the correct one. During the training process, we employed the entropy minimization technique until all the leaves of the tree became homogeneous. After having the decision tree trained, decision making is performed quickly. Finally, a binary image is obtained, where the inner dark regions have to be localized.

Step MCT4 - Region growing and selection

The identification of dark spots situated within the light area of the binary image, is performed by an iterative region growing method. As long as there are dark pixels in the segmented image, a dark pixel is arbitrarily chosen and a region is grown around it. Outer space (which is also dark) is obviously discarded, and the detected dark spots are

separately stored. Each branch of the root canal, which is present in the cross section, should normally be represented by a single dark region within the slice. Unfortunately, mostly because of imaging artifacts or complex shaped canals, there are some cases, when a single canal branch is manifested by more than one dark region. These cases can be detected automatically, but their treatment sometimes requires manual intervention.

Each dark spot has its center point, which can be computed two different ways: 1) as the center of gravity of the spot; 2) by means of morphological thinning. The center of gravity is easier to compute, but sometimes falls outside the spot. Morphological thinning always gives a quasi-centrally located center point, but entails more computational load.

The automatic selection of detected spots can be performed by several different protocols, which are summarized in Table 1. Protocol P1 can be used in cases of incisor teeth only, when a priori anatomical information makes the presence of a single spot highly probable.

Step MCT5 - Automatic shape regularization

Due to the artifacts present in the original micro-CT records, the dark spot detected in certain slices may contain irregularities. There are several kinds of such cases: some can be treated by automatic regularization techniques, while there are also cases that require manual interaction. For example, a light "island" within the dark spot is easily removable. Strange shaped "peninsulas" can be treated by large masked median filter or morphological opening/closing. There are also cases where the real root canal is detected as several separate dark spots situated very close from each other, which need to be unified. Automatic unification is possible using morphological operations or distance transform.

Step MCT6 - Correlation checking

The accurate segmentation of the micro-CT images may demand manual intervention. Fortunately, the necessity of such steps is visible from the correlation of detected dark spots within adjacent cross sections. Other words, there cannot be a relevant change in the structure found within neighbor slices. Wherever there is a large distance between the center points detected in neighboring slices (see for example Figure 3), either we have a bifurcation, or some intervention is likely to be beneficial. In case of bifurcation, the number of dark spots in the neighbor slices should differ, but correlate with the next neighbor slice for each point. Thus, detecting the need for manual intervention is automated in the proposed process.

Step MCT7 - Manual interactions to improve accuracy

The user has the opportunity to change the result of the automatic segmentation within any of the slices. As it was justified in the previous section, the user is advised where the interaction is required. This means that the algorithm automatically detects the cases

Table 1 Implemented spot selection protocols

Name	Description
P1 - Only one spot	Always extracts the largest dark spot from the slice.
P2 - At most two/three/four	Extracts the second/third/fourth spot if it is present and larger than a small threshold size.
P3 - Adaptive	It may extract any number of spots, according to some predefined rules that concern the size of different spots.

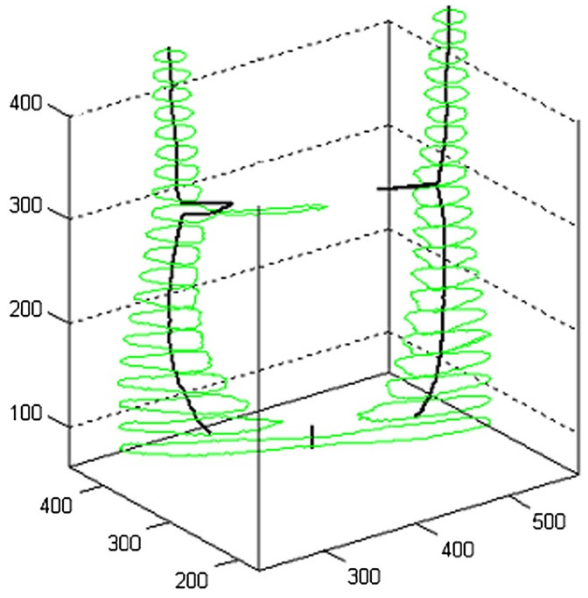

Figure 3 Checking the correlation of dark spot centers in neighbor slices. It can reveal the presence of bifurcations (around slice 70) and the need for manual interaction (around slice 310). Both events can be localized and identified automatically.

when the manual intervention is likely to be beneficial and asks for manual intervention. The implemented manual interventions are summarized in Table 2.

Step MCT8 - Reconstruct the spatial shape of the root canal

The inner dark spots localized within each slice are put together in space to form a three dimensional object that describes the shape of the root canal. The center line of this object will be searched for using a procedure based on 3D curve skeleton extraction.

Step MCT9 - 3D curve skeleton extraction

As mentioned in [22], there are various approximation algorithms for the 3D curve skeleton of voxelized objects. We need to employ such an approach which provides a smooth curve with low amount of branches, and extremely insensitive to zigzagged surfaces. This sort of curve skeleton is reportedly produced by potential field methods. The actual skeleton extraction algorithm implemented into the medial line identification procedure is the hierarchical formulation of the potential field based problem, described in [30].

Table 2 List of implemented manual interventions

Name	Description
M1	Overrule the decision dictated by the decision tree.
M2	Change the local threshold to any desired value.
M3	Discard some of the automatically detected dark spots.
M4	Unify several dark spots using a parametric active contour model (snake) initialized by the user.

Step MCT10 - Corrections of the extracted skeleton

The 3D curve skeleton accurately handles critical cases like root canal bifurcations, or slices that are far from being orthogonal to the root canal's direction. Under such circumstances, the curve skeleton is an excellent approximation of the center line. However, at all endings of the root canal, the curve skeleton is either shorter than it should be as the iterative thinning has its effect from every direction, or it has several short branches connected to high curvature points of the surface of the reconstructed 3D object.

To produce an accurate center line with the skeleton extraction algorithm, the divergence parameter of Cornea's potential field approach must be chosen to be low enough so that the endings of the skeleton towards superficial high curvature points are not present. Further, to avoid the shortened endings of the skeleton, we need to virtually lengthen all endings of the reconstructed tubular 3D object with as many slices (identical to the peripheral one) as necessary. The number of such virtually added slices is well approximated as the shortest radius of the dark spot in the peripheral slice.

Most steps of the algorithm summarized in Figure 2 are performed automatically. Only the box drawn with dotted line comprises any possible manual interactions. This step is not mandatory in simple cases, such as incisor teeth or images with low amount of artifacts.

Processing cone-beam CT records

Cone-beam CT image volumes usually consist of hundreds of parallel equidistant slices, each slice being a single-channel intensity image (some examples are shown in Figure 4). Voxels are isovolumetric, having their size between $100-300\mu$m. At such a low resolution, the root canals frequently have the width of single or a few voxels, and in order to have accurate identification, partial volume effect has to be handled properly. Voxel intensities are recorded as absolute values in Hounsfield units (HU).

Step CBCT1 - Image enhancement

The signal-to-noise ratio is in direct proportion with the X-ray dose received by the scanned patient. As the dose should be kept minimal [5], the noise level in the image volume is frequently high. Under such circumstances, an efficient filtering technique needs to be applied to reduce the adverse effect of high frequency noise upon segmentation,

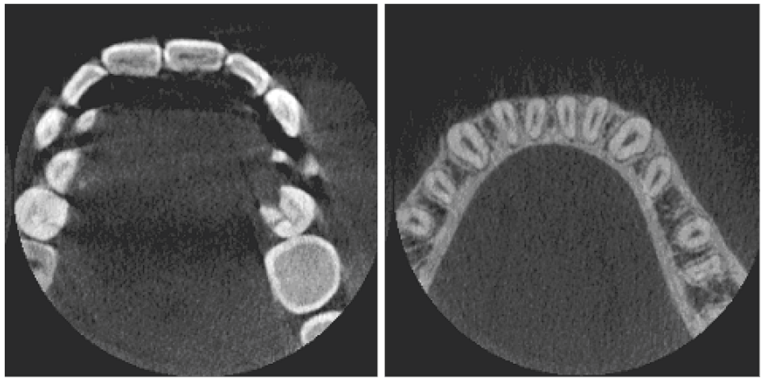

Figure 4 Examples of slices from CBCT volumes.

without altering or significantly reducing detectable edges. To perform this operation, the context sensitive averaging filter proposed in [31] is employed.

Step CBCT2 - Segmentation

Region growing methods usually start from a seed point and grow homogeneous regions around it, by including those neighbor voxels into the region that satisfy a predefined homogeneity criterion. The most frequently used homogeneity criterion is based on voxel intensities, and usually states that a region is homogeneous whenever the standard deviation of voxel intensities within the region is below a predefined threshold. Such segmentation methods frequently have difficulties in noisy environments. High frequency noises can yield several few-voxel regions, while intensity inhomogeneity also hinders the formation of large continuous regions.

The proposed segmentation method is very similar to the classical region growing approach, but there is an important difference that enables it to grow regions beyond noisy voxels. The proposed method is defined as follows.

Let $X = \{x_1, x_2, \ldots, x_N\}$ be the set of voxels in the image volume, where N represents the number of voxels. A fuzzy subset of X is defined as a set of ordered pairs:

$$F = \{(x_i, \mu_F(x_i)) | i = 1 \ldots N\}, \tag{1}$$

where $\mu_F : X \rightarrow [0, 1]$ is called the membership function F in X. We can define a fuzzy relation in X as a fuzzy subset of X^2 written as:

$$\Psi = \{((x_i, x_j), \mu_F(x_i, x_j)) | i, j = 1 \ldots N\}, \tag{2}$$

with $\mu_\Psi : X^2 \rightarrow [0, 1]$. The so-called α-cut of a fuzzy subset F is the crisp set:

$$X_\alpha^{(F)} = \{x \in X | \mu_F(x) \geq \alpha\}. \tag{3}$$

The fuzzy relation Ψ_α is called a fuzzy link between x_i and x_j, if:

$$\exists \alpha \in (0, 1] : \mu_\Psi(x_i, x_j) \geq \alpha. \tag{4}$$

If a fuzzy relation Ψ_α holds over a set $X = \{x_1, x_2, \ldots, x_N\}$, then we may write $x_i \Psi_\alpha x_j \; \forall x_i, x_j \in X$.

Two elements x_i and x_j of a set X are α-chained, if there exists a sequence of fuzzy linked elements $\xi_1, \xi_2, \ldots, \xi_k$ in X, such as:

$$x_i \Psi_\alpha \xi_1 \Psi_\alpha \xi_2 \Psi_\alpha \ldots \Psi_\alpha \xi_{k-1} \Psi_\alpha \xi_k \Psi_\alpha x_j. \tag{5}$$

In the proposed segmentation algorithm, two points will be in the same segment whenever they are α-chained through neighbor voxels. The only questions that remain are how to define the relation Ψ to distinguish voxels belonging to different types of tissues, and which is the right value of α that assures a suitable granularity of detected segments?

The goal is to detect a tooth (or a molar) as a single continuous 3D region, and the root canal as another volumetric region inside the tooth. To achieve the above goal, a fuzzy relation for the voxels needs to be defined reflecting the pairwise similarity between the two voxels. Two voxels should be similar if they are close to each other both in physical position and observed intensity.

Similarly to the coefficients of the context dependent filter defined in [31], a fuzzy relation Ψ is defined in such a way that it contains the product of two factors:

$$\mu_\Psi(x_i, x_j) = \delta(x_i, x_j) \times \sigma(x_i, x_j). \tag{6}$$

The first factor is a term that depends on the physical distance between the voxels: the closer two voxels are from each other, the more similar they are. The second factor reflects the similarity between the intensity of the two voxels. Here again, equal intensities have the highest similarity, and the larger the difference in intensities, the lower is the degree of similarity.

Two terms are thus defined according to the following rules:

$$\delta(x_i, x_j) = \frac{1}{\sqrt{1 + \kappa_\delta d(x_i, x_j)}}. \tag{7}$$

$$\sigma(x_i, x_j) = \frac{1}{\sqrt{1 + \kappa_\sigma |\log \frac{v(x_i)}{v(x_j)}|}}. \tag{8}$$

Trade-off parameters κ_δ and κ_σ enable fine tuning the behavior of the segmentation algorithm. High values of κ_δ reduces the proposed method to conventional region growing, while low values enable the algorithm to join regions of similar intensity, which are not physically connected. High values of κ_σ determine the algorithm to create regions of piecewise constant intensity, while low ones enable regions to swallow neighbor voxels whose intensity significantly differs from the intensity of the region.

Step CBCT3 - 3D object reconstruction

From the segmented image volume, the outer surface of molars and incisors is performed by the corrected version of the marching cube method [32]. This is also employed to reconstruct the shape of the root canal. All surfaces are obtained as triangulated mesh.

Step CBCT4 - Medial line extraction

Medial lines of tubular structures are often modeled by 3D curve skeletons [22]. Potential field based methods [27] usually assure smooth curve skeletons of better quality, but they need a much higher resolution of the object. For cone-beam CT volumes, the low resolution of images does not allow employing potential field based curve skeleton extraction methods. As the surface of the root canal is reconstructed as a mesh, it was straightforward to choose to apply the so-called 3D curve skeleton extraction via mesh contraction [33].

Results

Accuracy tests

The micro-CT image processing procedure was tested on 25 image volumes that included 17 incisors and 8 molars.

Figure 5 exhibits the intermediary results provided by the 2D segmentation. Three cases of various difficulties are presented in the three rows of the image. The first row presents a simple case involving a slice with two dark spots representing two different, easily detectable root canals (there was a bifurcation several slices away from this one). The slice in the middle row manifests an odd shaped dark region, which was successfully detected. The slice presented in the third row shows a difficult case: three different dark spots are present in the segmented images, but they belong to only two different canal branches. This is the case that requires correlation test with neighbors or decision overruling performed by the ANN. Figure 6 shows intermediary results at various points of the process.

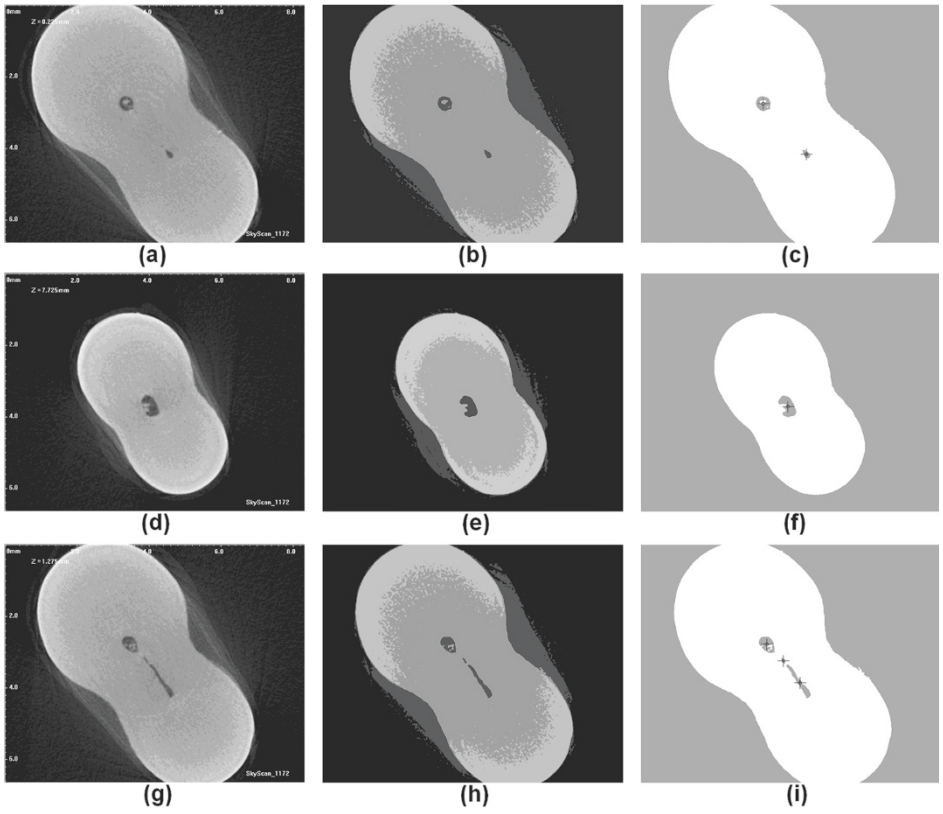

Figure 5 Detailed view of image segmentation in 2D. Each row represents a different slice. First column shows the original recorded images; second column presents the clustered images (4 clusters); last column indicates the segmented binary images with detected center points.

Figure 7 shows four different 3D views of a root canal, together with its detected medial axis. The central line was produced from 944 equidistant slices, segmented in 2D with binary separation using the global optimal threshold.

The CBCT volume processing procedure was tested on 36 image volumes that contained incisors and molars in equal number. The proposed algorithm requires a single interaction: the user is asked to mark the tooth (incisor or molar) desired to be segmented. The volume of interest is then processed automatically.

The surface of segmented teeth and root canals are produced as mesh. After the automatic processing, the user may also visualize sectioned views of the tooth. Figure 8 exhibits some views produced in case of an incisor, while Figure 9 shows the result provided in case of a molar with three branches in the root canal. In both these figures, part

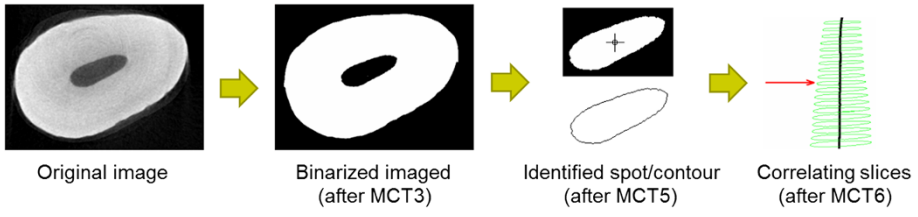

Figure 6 Intermediary results of micro-CT image processing.

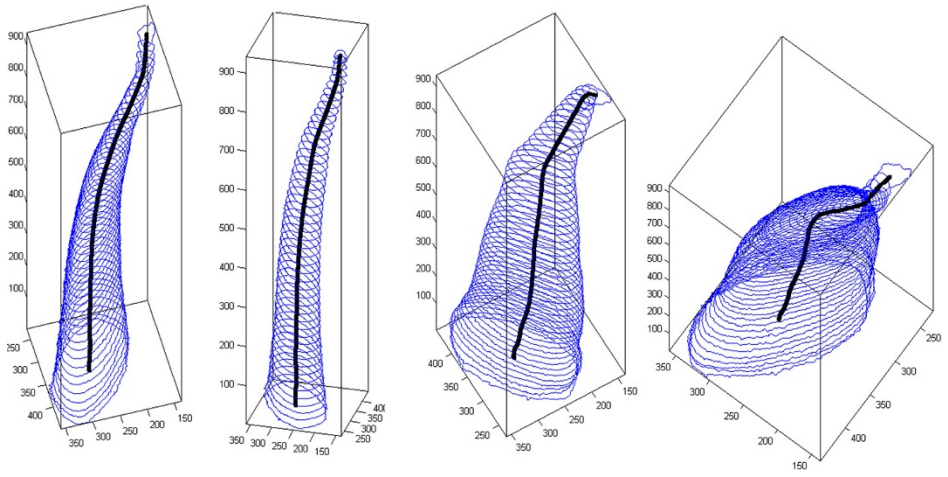

Figure 7 Various 3D views of a root canal, with the extracted medial line. Numbers indicate voxels, which are easily convertible to millimeters.

(a) shows the shape of the tooth, (b) the shape of the root canal, represented at the same scale, in vertical position correlated with (a). Images shown in (c) and (d) are various sectioned views of the tooth and root canal, visualized together.

Figure 10 presents the extracted central line in case of an incisor, together with the shape of the root canal and the shape of the tooth. All three images represent the same tooth, visualized from different angles. Sections of the tooth are shown using elevated contour plots, green contours indicating the shape of the tooth, and red ones the shape of the detected root canal. Indicated coordinates represent distances in voxels, which are easily convertible to millimeters.

Figure 11 shows two different versions of a segmented molar, using the same representation conventions: the image on the left side, having shortened roots and root canals, is obtained automatically, while the image on the right is the correct segmentation obtained after manual intervention. The simple intervention was needed to inform the algorithm that four distinct volumetric regions that were automatically detected, in fact belong together to form a whole molar.

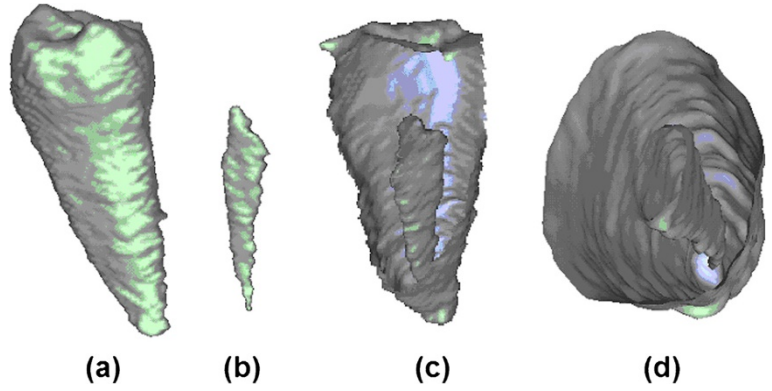

Figure 8 Various reconstructed views of an incisor and its root canal: (a) shape of the incisor; (b) shape of the root canal; (c)-(d) sectional views.

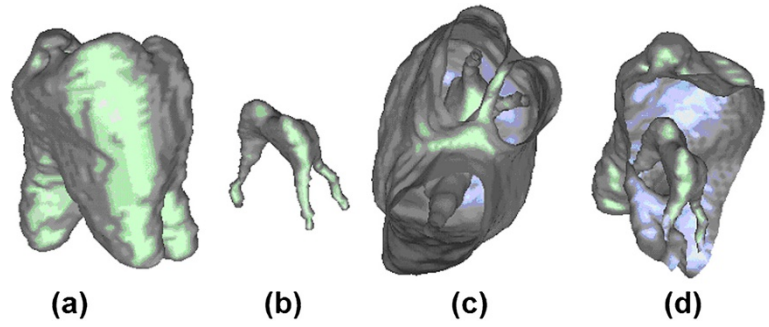

Figure 9 Various reconstructed views of a molar and its bifurcated root canal: (a) shape of the molar; (b) shape of the root canal; (c)-(d) sectional views.

The accuracy of the segmentation is usually better in case of incisors than in case of molars, because the latter have more details to identify. The main difficulty comes from the low resolution of the CBCT imaging technology, which makes some structures have tiny sizes, sometimes under the unit size of a voxel. The identification of the medial line is efficient and accurate: as the width of the root canal hardly ever exceeds 10 voxels, the mesh contraction algorithm finishes the extraction of the curve skeleton in 7-8 iterations. The identified skeleton is smooth, centrally located, and its bifurcations are suitable to model the actual shape of root canal branches.

Both proposed procedures can automatically and accurately process more than 90% of the recorded image sets, while the rest of the cases need serious amount of manual interaction. The MCT procedure was tested on 25 image volumes. In case of two molars, several uncorrelated neighbor slices were found, where the necessity of manual interaction could not be accurately detected. In the other 23 volumes, a total number of 227 (out of 23391) slices were advised for expert inspection, but only 119 of them required actual intervention. This amount of false positives is acceptable. The correlation between the automatic decisions made by the developed algorithm and the expert validating the algorithm is shown in Table 3.

Out of 36 image volumes used for testing the CBCT procedure, 29 led to correct segmentation and identification of the root canal without needing any automatic interaction. In case of 7 molars, manual interaction was needed, being able to solve 4 of them, similarly

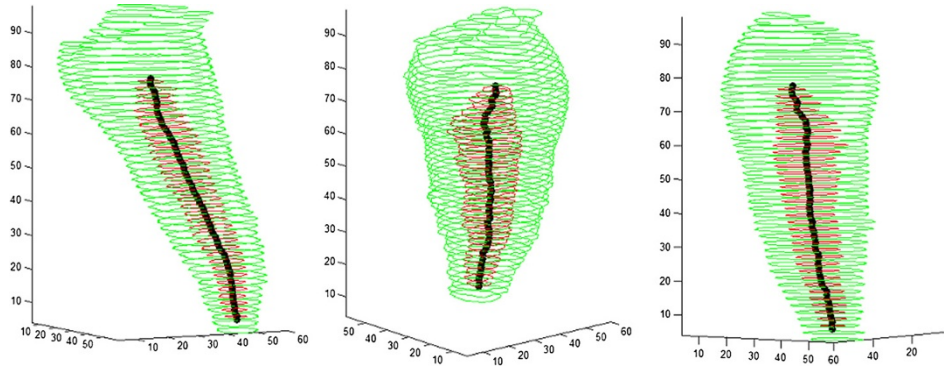

Figure 10 Various 3D views of a root canal having no bifurcation, with the extracted medial line.

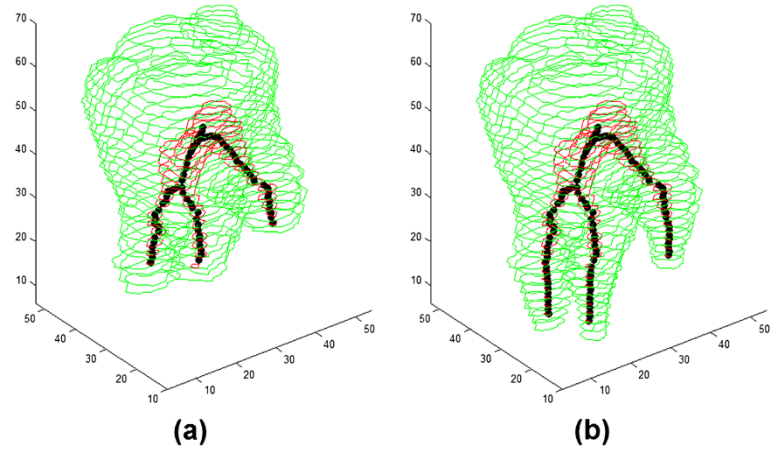

Figure 11 3D views of a molar with its bifurcated root canal and the extracted medial line: (a) before and (b) after manual intervention.

to the case exhibited in Figure 11. The quantitative validation results of the two developed algorithms are shown in Table 4.

The proposed procedures provide useful information for mathematical description of the root canal's shape. The medial line can be successfully approximated by spline curves, as described in [34,35].

Efficiency

Using a i5-processor PC, the processing of a micro-CT slice in 2D lasts 0.2-0.3 seconds, while a central canal reconstruction is performed in less than a second. The extraction of 3D curve skeleton representing the canal's medial axis requires 10-15 seconds, depending on the number of voxels in the canal's volume. On the other hand, having roughly $0.5 - 1.5 \times 10^6$ voxels in the volume of interest, the identification of a manually selected tooth in a CBCT volume automatically performs in less than a second.

Discussion

The key advantage of both algorithms is the high degree of automatic execution, and the ability of automatically detecting the necessity of manual interventions. In case of micro-CT records, the latter feature stems from checking the correlation between neighbor slices. Wherever the correlation is weak, it can be because of: (1) bifurcations of the root canal; (2) mistaken segmentation in 2D. The number, size and position of detected sections of the root canal, situated within the investigated neighbor slices, are the main

Table 3 Accuracy details of automatic detection of the need for manual intervention in the case of CBCT records

		Expert evaluation	
		No need for intervention	**Intervention needed**
Automatic detection	**No need for intervention**	23150	14
	Intervention needed	108	119

Table 4 Quantitative results of validation

Description	Micro-CT	CBCT
Total test image volumes	25	36
Successfully processed image volumes	23	33
Overall success rate	92.0%	91.7%
Overall success in incisors	100.0%	100.0%
Overall success in molars	75.0%	83.3%
Minimum processing time	288 sec	0.69 sec
Average processing time	341 sec	0.93 sec
Maximum processing time	490 sec	1.61 sec

data for the decision. In case of CBCT records, steps CBCT2 identifies piecewise continuous volumetric regions that belong to the dentin, which are reconstructed to form the tooth in Step CBCT3. There are cases, when unifying these volumetric regions is not obvious. In such cases, without manual interventions, we may lose the inferior, narrow part of the root canal branches. However, manual intervention can help us out in these cases as well (see Figure 11).

An essential tool in the MCT procedure is the decision tree implemented in Step MCT3, responsible for the correct outcome of the 2D segmentation. The training data set consisting of 250 images, was selected from seven image volumes, through an automated process. Those images were selected as suitable candidates, for which the two EnFCM-based segmentations ($c = 2$ and $c = 4$) did not correlate in any combination of the classes. Using the test image set of 25 volumes of approx. 1000 slices each, the decision learnt from 250 training images proved acceptable, in the sense that less than 0.1% of the slices needed manual intervention due to the wrong decision of the tree.

The developed procedures certainly have some limitations, too. The reduced amount of image data originating from a single CT imaging system, which was used for the creation of the procedures, certainly could not cover all typical root canal deformations. A larger amount of images would definitely make the system more stable and its decisions more robust.

Conclusions

We have proposed and implemented two complex image processing procedures for detecting the center line from dental micro-CT and CBCT records. Both procedures work predominantly automatically, providing the opportunity for the user to improve the outcome using some optional manual interventions only where needed.

The proposed image processing procedures are validated on real micro-CT and CBCT images. Over 90% of the test data set was segmented and identified automatically and correctly. The identified center lines are accurate and suitable for further mathematical modeling (e.g. spline curve fitting). Thus, this research has created and validated the image processing systems and corresponding image processing methods to efficiently assist common dental interventions.

Abbreviations

CT: Computed Tomography; CBCT: Cone-beam Computed Tomography; FCM: Fuzzy c-means; 2/3 D: two/three dimensional, EnFCM: Enhanced Fuzzy c-means; ANN: Artificial Neural Network.

Competing interests

The authors declare that they have no competing interests.

Acknowledgements
The author would like to express his thanks for Prof. Csaba Dobó-Nagy (Semmelweis University, Budapest) for providing the clinical data set used for validation as well as for Dr. László Szilágyi for his consultancy and his help in the implementation of the algorithms. This research supported by the Hungarian National Scientific Research Foundation, Grants No. CK80316 and K82066, and it is connected to the scientific program of the New Széchenyi Plan (Project ID: TÁMOP-4.2.1/B-09/1/KMR-2010-0002).

Received: 23 July 2012 Accepted: 16 October 2012
Published: 29 October 2012

References

1. Peters OA: **Current challenges and concepts in the preparation of root canal systems: a review.** *J Endodontics* 2004, **30:**559–567.
2. Swain MV, Xue J: **State of the art of micro-CT applications in dental research.** *Int J Oral Sci* 2009, **1:**177–188.
3. Scarfe WC, Farman AG, Sukovic P: **Clinical applications of cone-beam computed tomography in dental practice.** *J Can Dent Assoc* 2006, **72:**75–80.
4. Scarfe WC, Levin MD, Gane D, Farman AG: **Use of cone beam computed tomography in endodontics.** *Int J Dent* 2009, **2009**(634567):1–20.
5. European Commission, Directorate-General for Energy, Directorate D – Nuclear Energy, Unit D4 –Radiation Protection: *Radiation Protection No. 172. Cone Beam CT for Dental and Maxillofacial Radiology: Evdence Based Guidelines*. Europe; 2012.
6. Analoui M, Krisnamurthy S, Brown C: **Modeling and measurement of root canal using stereo digital radiography.** *Proc SPIE Int Soc Opt Eng* 2000, **3976:**306–314.
7. Hong SY, Dong J: **3-D root canal modeling for advanced endodontic treatment.** *Proc SPIE Int Soc Opt Eng* 2002, **4702:**321–330.
8. Endo M, Kobashi S, Kondo K, Hata Y: **Dentistry support ultrasonic system for root canal treatment aided by fuzzy logic.** In *Proceedings of the IEEE International Conference on Systems, Man and Cybernetics, 12-15 October 2005; Hawaii*; 2005:1494–1499.
9. Lee JK, Ha BH, Choi JH, Perinpanayagam H: **Quantitative three-dimensional analysis of root canal curvature in maxillary first molars using micro-computed tomography.** *J Endodontics* 2006, **32:**941–945.
10. Willershausen B, Kasaj A, Röhrig B, Marroquin BB: **Radiographic investigation of frequency and location of root canal curvatures in human mandibular anterior incisors in vitro.** *J Endodontics* 2008, **34:**152–156.
11. van Soest, G, Shemesh H, Wu MK, van der Sluis, L W M, Wesselink PR: **Optical coherence tomography for endodontic imaging.** *Proc SPIE Int Soc Opt Eng* 2008, **6843**(68430F):1–8.
12. Germans DM, Spoelder HJW, Renambot L, Bal HE, van Daatselaar S, van der Stelt P: **Measuring in virtual reality: a case study in dentistry.** *IEEE Trans Instrum Meas* 2008, **57:**1177–1184.
13. Park JW, Lee JK, Ha BH, Choi JH, Perinpanayagam H: **Three-dimensional analysis of maxillary first molar mesiobuccal root canal configuration and curvature using micro-computed tomography.** *Oral Surgery, Oral Medicine, Oral Pathology, Oral Radiology, and Endodontology* 2009, **108:**437–442.
14. Neves AA, Coutinho E, Cardoso MV, Jaecques SV, van Meerbeek, B: **Micro-CT based quantitative evaluation of caries excavation.** *Dental Materials* 2010, **26:**579–588.
15. Verma P, Love RM: **A Micro CT study of the mesiobuccal root canal morphology of the maxillary first molar tooth.** *Int Endodontic J* 2011, **44:**210–217.
16. Yamada M, Ide Y, Matsunaga S, Kato H, Nakagawa KI: **Three-dimensional analysis of mesiobuccal root canal of Japanese maxillary first molar using micro-CT.** *Bulletin of Tokyo Dental College* 2011, **52:**77–82.
17. Kaya S, Adiguzel O, Yazuv I, Tumen EC, Akkus Z: **Cone-beam dental computerized tomography for evaluating changes of aging in the dimensions central superior incisor root canals.** *Medicina Oral, Patologia Oral, y Cirugia Bucal* 2011, **16:**e463–e466.
18. Li KZ, Gao Y, Zhang R, Hu T, Guo B: **The effect of a manual instrumentation technique on five types of premolar root canal geometry assessed by micro-computed tomography and three-dimensional reconstruction.** *BMC Medical Imaging* 2011, **11:**14.
19. Frisardi G, Chessa G, Barone S, Paoli A, Razionale A, Frisardi F: **Integration of 3D anatomical data obtained by CT imaging and 3D optical scanning for computer aided implant surgery.** *BMC Medical Imaging* 2011, **11:**5.
20. Li H, Yezzi A, Cohen L: **3D multi-branch tubular surface and centerline extraction with 4D iterative key points.** *Lect Notes Comp Sci* 2009, **5762:**1042–1050.
21. Dong J, Hong SY, Hasselgren G: **Theories and algorithms for 3-D root canal model construction.** *CAD Computer Aided Design* 2005, **37:**1177–1189.
22. Cornea ND, Silver D, Min P: **Curve-skeleton properties, applications, and algorithms.** *IEEE Trans Vis Comp Graph* 2007, **13:**530–548.
23. Ma CM, Sonka M: **A fully parallel 3D thinning algorithm and its applications.** *Comp Vis Imag Understand* 1996, **64**(3):420–433.
24. Palágyi K, Kuba A: **A parallel 3D 12-subiteration thinning algorithm.** *Graphical Models and Image Processing* 1999, **61**(4):199–221.
25. Pudney C: **Distance-ordered homotopic thinning: a skeletonization algorithm for 3D digital images.** *Comp Vis Imag Understand* 1998, **72**(3):404–413.
26. Wu FC, Ma WC, Liang RH, Chen BY, Ouhyoung M: **Domain connected graph: the skeleton of a closed 3D shape for animation.** *The Visual Computer* 2006, **22:**117–135.
27. Cornea ND, Silver D, Yuan X, Balasubramanian R: **Computing hierarchical curve-skeletons of 3D objects.** *The Visual Computer* 2005, **21:**945–955.
28. Szilágyi L, Benyó Z, Szilágyi SM, Adam HS: *MR brain image segmentation using an enhanced fuzzy c-means algorithm*; 2003.

29. Bezdek JC: *Pattern Recognition with Fuzzy Objective Function Algorithms*. New York, NY: Plenum; 1981.
30. Szilágyi L, Szilágyi SM, Iclănzan D, Szabó L: **Efficient 3D curve skeleton extraction from large objects.** *Lect Notes Comp Sci* 2011, **7042:**133–140.
31. Szilágyi L, Szilágyi SM, Benyó Z: **A modified fuzzy c-means algorithm for MR brain image segmentation.** *Lect Notes Comp Sci* 2007, **4633:**866–877.
32. Nielson GM, Hamann B: **The asymptotic decider: resolving the ambiguity in marching cubes.** In *Proceedings of the 26th IEEE Conference on Visualization, 22-25 October 1991; Tempe, AZ*; 1991:83–91.
33. Au OKC, Tai CL, Chu HK, Cohen-Or D, Lee TY: **Skeleton extraction by mesh contraction.** *ACM Trans Graph* 2008, **27**(44):1–10.
34. Dobó-Nagy C, Szabó J, Szabó J: **A mathematically based classification of root canal curvatures on natural human teeth.** *J Endodontics* 1995, **21**(11):557–560.
35. Dobó-Nagy C, Keszthelyi G, Szabó J, Sulyok P, Ledeczky G, Szabó J: **A computerized method for mathematical description of three-dimensional root canal axis.** *J Endodontics* 2000, **26**(11):639–643.

doi:10.1186/1475-925X-11-81
Cite this article as: Benyó: Identification of dental root canals and their medial line from micro-CT and cone-beam CT records. *BioMedical Engineering OnLine* 2012 **11**:81.